SANDIA REPORT
SAND2022-1360
Printed February 2022

Sandia National Laboratories

Effects of Model Uncertainties in Underground Chemical Explosions on Far-field Results

Mehdi Eliassi and Leiph A. Preston

Prepared by
Sandia National Laboratories
Albuquerque, New Mexico
87185 and Livermore,
California 94550

Issued by Sandia National Laboratories, operated for the United States Department of Energy by National Technology & Engineering Solutions of Sandia, LLC.

Available to DOE and DOE contractors from

U.S. Department of Energy
Office of Scientific and Technical Information
P.O. Box 62
Oak Ridge, TN 37831

Telephone: (865) 576-8401
Facsimile: (865) 576-5728
E-Mail: reports@osti.gov
Online ordering: http://www.osti.gov/scitech

Available to the public from

U.S. Department of Commerce
National Technical Information Service
5301 Shawnee Rd
Alexandria, VA 22312

Telephone: (800) 553-6847
Facsimile: (703) 605-6900
E-Mail: orders@ntis.gov
Online order: https://classic.ntis.gov/help/order-methods/

ABSTRACT

We used the CTH shock physics code to simulate the explosion of an 18-t chemical explosive at a depth of 250 m. We used the CTH in the two-dimensional axisymmetric (cylindrical) geometry (2DC) and most simulations included fully tamped explosions in wet tuff. Our study focused on parametric studies of three of the traditional strength models available in CTH, namely, geologic-yield, elastic perfectly-plastic von Mises, and Johnson-Cook strength (flow stress) models. We processed CTH results through a code that generates Reduced Displacement Potential (RDP) histories for each simulation. Since RDP is the solution of the linear wave equation in spherical coordinates, it is mainly valid at far-enough distance from the explosion the elastic radius. Among various parameters examined, we found the yield strength to have the greatest effect on the resulting RDP, where the peak RDP reduces almost linearly in log-log space as the yield strength increases. Moreover, an underground chemical explosion results in a cavity whose final diameter is inversely proportional to the material yield strength, i.e., as the material's yield strength increases the resulting final cavity radius decreases. Additionally, we found the choice of explosive material (COMP-C4 versus COMP-B) has minor effects on the peak RDP, where denser COMP-C4 shows higher peak RDP than the less dense COMP-B by a factor of ~1.1. In addition to wet tuff, we studied explosions in dry tuff, salt, and basalt, for a single strength model and yield strength value. We found wet tuff has the highest peak RDP value, followed by dry tuff, salt, and basalt. 2DC simulations of explosions in 11 m radius spherical, hemispherical, and cylindrical cavities showed the RDP signals have much lower magnitude than tamped explosions, where the cavity explosions mimicked nearly decoupled explosions.

ACKNOWLEDGEMENTS

This research was funded by the National Nuclear Security Administration, Defense Nuclear Nonproliferation Research and Development (NNSA DNN R&D). The authors acknowledge important interdisciplinary collaboration with scientists and engineers from LANL, LLNL, MSTS, PNNL, and SNL. This paper describes objective technical results and analysis. Any subjective views or opinions that might be expressed in the paper do not necessarily represent the views of the U.S. Department of Energy or the United States Government. We would like to thank Seth Root (Sandia National Laboratories) for providing his RDP solver tool that greatly helped in analyzing our modeling and simulations results.

CONTENTS

LIST OF FIGURES

LIST OF TABLES

This page left blank

ACRONYMS AND DEFINITIONS

Abbreviation	Definition
2DC	Two Dimensional Cylindrical
AMR	Adaptive Mesh Refinement
DOB	Depth of Burial
DYDP	Slope parameter in GEO model
EOS	Equation of State
EPPVM	Elastic Perfectly-Plastic von Mises Yield Surface Model
GEO	Geological yield strength model
JC	Johnson-Cook strength and damage models
JWL	Jones-Wilkins-Lee
MAXL	User-defined maximum allowable level mesh refinement in AMR.
RDP	Reduced Displacement Potential
TVBC	time varying boundary condition
Yinf	Yield strength parameter in GEO model

1. INTRODUCTION

In our previous studies, we used the CTH Eulerian shock physics code (Schmitt 2017) to compute ground motion and stress data at many stationary tracers as the Time Varying Boundary Conditions (TVBC). The TVBCs are used by the linear seismic code axiElasti to generate seismic signals, e.g., see Preston, et. al. (2021) and Preston, et. al. (2008) for a description of the axiElasti code. Our prior research has evaluated the effects of various geologic materials, as well as material yield values for a single flow stress model (often referred to as the material strength model) on linear seismic source time function inversions. However, in the absence of experimental data to validate our computational methods, it is necessary to explore the various physical (constitutive models, equations-of-state, etc.) and numerical (choice of meshing, geometry, and domain size) parameters and their effects on key signatures (i.e., seismic signal generated following underground explosions). For instance, in Preston, et. al. (2021), we showed that different yield strength values for a single model greatly affect the resulting source time function. Our previous work, however, did not explore the effects of various strength models and their various parameters, which is the starting point for identifying key parameters needed to eventually quantify parameter uncertainties when experimental data becomes available. Since the process of the one-way coupling between CTH and axiElasti through the TVBC can be time and computationally intensive, for this study we considered a simpler approach by post-processing the CTH results (for a limited number of stationary tracers) using an in-house code developed to generate Reduced Displacement Potential (RDP) time histories (explained in detail in Section 2 of this report). As we will discuss, RDP is not a replacement of the TVBC approach, as the RDP primarily assumes that the seismic signal can be analyzed beyond a so-called elastic radius where ground motion is "elastic" and that the Earth is homogeneous. The RDP approach, thus, allows us to process many CTH results more quickly where we explore various parameter spaces. Again, *our ultimate motivation is to identify key models (e.g., strength and damage) and the parameters that control the response from an underground chemical explosion. Moreover, the current study does not focus on uncertainty quantification (UQ) of these parameters. We hope to conduct UQ studies in a future work, where we can identify relevant measured data*.

1.1. Organization of This Report

This report is organized as follows:

Section 2 provides a short description of the concept of the Reduced Displacement Potential (RDP) as a surrogate for seismic analyses of our modeling and simulations results. Section 3 describes our basic computational model that consists of an 18-t tamped COMP-C4 explosion at a depth of 250 m in wet tuff material. Section 4 introduces the mathematical forms for the Jones-Wilkins-Lee (JWL) equation of state (EOS) that we use to model the explosive burn, and three material strength models, namely, the Geological-Yield Surface (GEO), Elastic Perfectly-Plastic von Mises (EPPVM) constant yield surface, and Johnson-Cook (JC) flow stress and damage models. Section 5 primarily focuses on simulations results based on the GEO strength model. The various subsections in this section discuss the effects of fracture pressure, mesh resolution, yield strength and slope parameters in the GEO model, choice of explosive materials (i.e., COMP-C4 compared to COMP-B), and finally the effects of EPPVM and JC strength models compared to the GEO model for COMP-B explosions in wet tuff. Section 6 compares the computed RDPs for other geologic materials, namely, basalt, salt, and dry tuff, to our baseline wet tuff materials using the GEO model for a single yield strength and COMP-B as the

explosive. Section 7 discusses the effects of explosions in spherical, hemi-spherical, and cylindrical cavities. Finally, Section 8 provides a few key conclusions from our modeling and simulations studies and makes recommendations for future studies.

2. REDUCED DISPLACEMENT POTENTIAL

As Latter et. al. (1959) and Heusinkvel (1981) discuss, the Reduced Displacement Potential (RDP) is the solution for a spherically expanding wave outgoing from the explosion source within a homogeneous material. Assuming the potential is independent of the distance (i.e., far enough away from the explosion source, where the media can be treated as elastic), we can state:

$$-\delta(t) = \frac{\partial\, \phi(\tau)}{\partial r \;\; r} \tag{1}$$

where $\delta(t)$ is the displacement as a function time, t, r is the radial distance, $\phi(\tau)$ is the potential, namely, RDP, and τ=t-r/c. Here, c represents the medium's compressional velocity. We can rewrite Eq. (1) as:

$$\delta(t) = \frac{\phi(\tau)}{r^2} + \frac{\phi'(\tau)}{rc} \tag{2}$$

where $\phi'(\tau)$ is the derivative of the potential function with respect to variable τ. As Patterson (1965) states, Eq. (2) can be numerically solved for the RDP, ϕ, for any form of displacement, $\delta(t)$, as long as $\delta(t)$ is chosen to be in the elastic region, again, far enough away from the explosion source.

To generate the RDP as a function of time, i.e., $\phi(t)$, we use a numerical solver provided by Seth Root[1]. Using that code, we read in the radial and axial velocity histories for any number of tracer points from our CTH (Schmitt 2017) simulations. The code then numerically integrates the time-varying radial velocity to find the displacement time history, $\delta(t)$, for all tracer points. However, since Eq. (2) is a linear non-homogenous ordinary differential equation, it is easy to show that its general solution is as follows:

$$\phi(\tau) = e^{-a\tau}\left[\int^{\tau} e^{a\chi}\delta(t)d\chi + k\right] \tag{3}$$

where a=c/r, χ is the integration variable, and k is an arbitrary integration constant. If we assume for t=0 (i.e., τ=-r/c), ϕ(-r/c) =0, we can then find constant, k, in Eq. (3). In fact, it is easy to show that for a constant displacement and compressional velocity, respectively, δ_0 and c_0 at a distance r=R_0, Eq. (3) simplifies to:

$$\phi(t) = R_0^2\delta_0\left[1 - e^{\left(-\frac{c_0 t}{R_0}\right)}\right] \tag{4}$$

Figure 1 compares the analytical solution in Eq. (4) to the numerical solution obtained from our RDP-solver. Here, we assumed δ_0=1 cm c_0=2.415 km/s, and R_0=100 m. Clearly, the analytic solution perfectly matches the numerical result, serving as a verification step of our RDP-solver code. Moreover, under such idealized conditions as considered here, RDP rises to a maximum value of $R_0^2\delta_0$=100 m^3 at roughly 0.2 sec and stays at that value. Of course, as we will show later, when the displacement varies with time, the shape of the RDP curve is more complicated.

[1] This code is developed in Jupyter Notebook framework, was provided to us by Seth Root (05912) and is available for distribution, if needed.

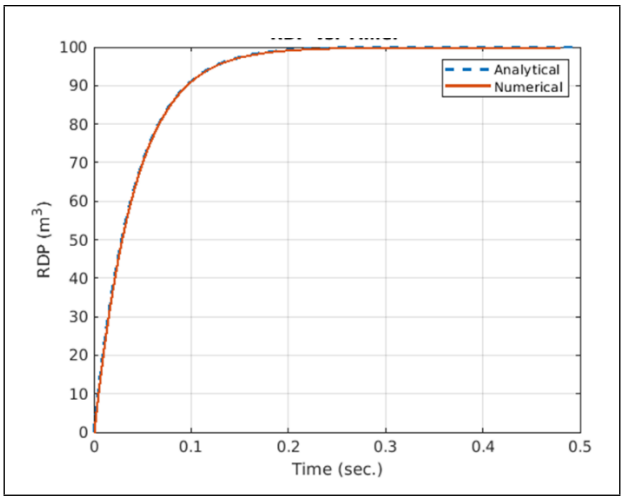

Figure 1. Comparison of the analytical solution of the RDP equation to that of numerical solution, for constant displacement.

Before leaving this section, it is important to remember that the RDP representation does not consider the free surface, inhomogeneous nature of the Earth, or other dissipative processes. That is, even in the purely elastic region, the interaction of the non-linear source with the far-field elastic region is complicated. That is why in our other studies by Preston et. al. (2021) the seismic response was evaluated based on time-varying boundary conditions (TVBC) that surrounded the non-linear region. In the current study, however, the RDP, i.e., solution of Eq. (2), serves as a convenient way for us to quickly assess a quasi-representation of the response of the nonlinear regime, as we perform our parametric studies to better understand and define sources of uncertainties in our modeling of underground explosions.

3. BASIC MODEL SETUP

Our baseline problem for simulating underground explosions consists of the detonation of a tamped sphere of 18 metric tons TNT equivalent of chemical explosive charge (either COMP-C4 or COMP-B), in wet tuff at a depth of burial (DOB) of 250 m. The detonation is modeled using Sandia's shock physics code CTH[2] (Schmitt 2017) in a two-dimensional axisymmetric cylindrical (2DC) geometry. The domain is discretized using Adaptive Mesh Refinement (AMR) approach, using the finest resolution of 12.5 cm. The problem domain is $0 \leq X \leq 1.28$ km and $-2.304 \text{ km} \leq Y \leq 0.256$ km, where X and Y refer to the radial and axial directions. It is worth noting that $-2.304 \text{ km} \leq Y \leq 0$ includes the ground material and $0 \leq Y \leq 0.256$ km is the air above the surface (i.e., $Y=0$). Here, we consider the ideal gas approximation for air. While we did examine the effects of tabular SESAME[3] air as well, we did not find any difference between ideal gas and SESAME air EOSs. The initial condition for the ground material uses 10^6 dynes/cm^2 (1 bar) pressure under gravitationally stable option resulting in a linear hydrostatic pressure distribution. The air above the ground (as well as the air in cavities, for cavity explosions) is assumed to be initially at a density of 0.001225 g/cc and temperature of 288 Kelvin (K).

Figure 2 shows the close-up view of the initial mesh (on the left side) and the charge (hot pink) on the right side. The grey background represents wet tuff. The EOS for wet tuff is based on the SESAME tabular EOS #7120 with an initial density of 1.95 g/cc (Kerley 1993). Here, we do not consider the effect of pore crush and thus porosity. As the figure shows there are ~11 mesh points across the explosive, which is a reasonable resolution for this problem. Our general refinement strategy is based on velocity magnitude of 0.1 m/sec. That is, as the resulting detonation shock front spreads into the surrounding material(s) and the velocity magnitude is above 0.1 m/sec, the mesh is refined to 12.5 cm. We discuss the effects of mesh refinement in Section 5.3.

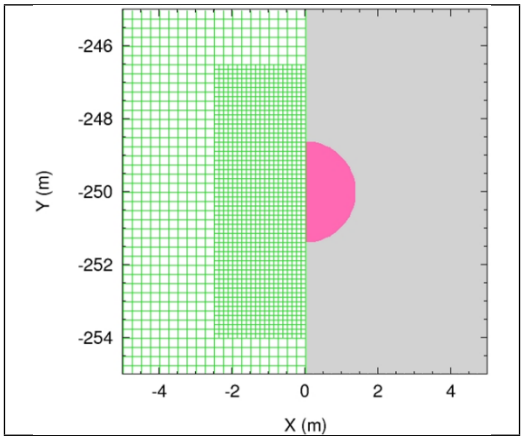

Figure 2. Close-up view of the baseline model setup. Right: COMP-C4 explosive charge with a radius of 139 cm (hot pink) and wet tuff (gray) and Left: initial mesh around and near the explosive charge.

[2] We used CTH Version 12.0 for all simulations reported in this work.
[3] Note that SESAME is not acronym and refers to a tabular database for the thermodynamic properties of materials (https://www.lanl.gov/org/ddste/aldsc/theoretical/physics-chemistry-materials/sesame-database.php)

Table 1 summarizes the various effects, along with the models, parameters (and parameter values) examined in this study. We note that the details of the models and/or parameters used are described in various section. However, this table is meant to provide an overall perspective of modeling and simulations in this report.

Table 1. List of physical and numerical effects studied in this work.

Effects	Model	Parameter	Parameter Values	Unit
Yield strength model	Geological-Yield Surface (GEO) strength model	Y_∞	0.01, 0.05, 0.1, 0.5, 1, and 5	Kilo bar (kb)
Slope/Nonlinearity	GEO	$\frac{dY}{dP}$ (DYDP)	-5,-2,-1,1,2,5	Dimensionless
Fracture pressure	Within the context of GEO model	P_{frac}	-0.025, -0.05, -0.1	kb
Mesh resolution	Adaptive Mesh Refinement (AMR)	MAXL	11 (6.25 cm), 10 (12.5 cm), 9 (25 cm)	Centimeters (cm) when referring to the mesh size
High-explosive material	JWL EOS	COMP-C4 and COMP-B	See Section 4.1 for details	
Yield strength model	Elastic Perfectly-Plastic von Mises (EPPVM)	Yield strength	0.05	kb
Yield strength model	Johnson-Cook strength and damage models	Various parameters affecting yield strength (i.e., flow stress) model	See Section 5.8 for details	

4. DESCRIPTION OF MAIN MODELS USED

This section provides the mathematical foundations for some of the models used in this work. The descriptions provided here are not meant to discuss the theoretical details and interested readers should refer to the appropriate citations for each model.

4.1. JWL Burn Model

We detonate the explosive charge from the center using the JWL EOS burn model. JWL is an analytic EOS that, as explained by Schmitt et al. (2017), "*is widely used to fit EOS for the detonation products of explosive*." Here, we present the basic form of the JWL EOS, along with the various parameters needed for the explosive materials. However, for additional discussion, we refer interested readers to Hertel (1998). For the JWL EOS, the relationships for pressure, P, and energy, E, as functions of density, ρ, and temperature, T, are usually stated as:

$$P(\rho,T) = A\, exp(-R_1 v) + B\, exp(-R_2 v) + \omega \rho C_v T \tag{5}$$

$$E(\rho,T) = \frac{1}{\rho_0}\left[\frac{A}{R_1}\, exp(-R_1 v) + \frac{B}{R_2}\, exp(-R_2 v) - \varepsilon_0\right] + C_v T \tag{6}$$

In Eq. (5) and (6), $v = \frac{\rho_0}{\rho}$ and ρ_0 is the initial density of the unreacted explosive. The constants A, B, R_1, R_2, ω, and ε_0 are experimentally determined, e.g., using a cylinder test, Schmitt et al. (2017), or from thermochemical models, in the absence of experimental data Hertel (1998). Finally, C_v refers to the constant volume specific heat. In this work, we used the standard values of the constants provided in CTH. **Table 2** lists the values for two explosives (used in this study) along with the detonation speed, D_{CJ} (which is a required input for the BURN model).

Table 2. JWL parameters for COMP-C4 and COMP-B reported in CTH.

Property	Explosive	
	COMP-C4	COMP-B†
ρ_0 (g/cc)	1.6	1.717
A (dyne/cm^2)	6.0977x10^{12}	5.242x10^{12}
B (dyne/cm^2)	1.295x10^{11}	7.678x10^{10}
R_1 (-)	4.5	4.2
R_2 (-)	1.4	1.1
ω (-)	0.25	0.34
ε_0 (erg/cm^3)	9x10^{10}	8.5x10^{10}
C_v (erg/gm-eV)	8.032x10^{10}	5.892x10^{10}
D_{CJ} (km/s)	8.193	7.979

† In CTH, COMP-B is called COMPB_GRADEA.

4.2. Geological-Yield Surface (GEO) Strength Model

Another important aspect of modeling the response of the geologic materials to an underground explosion is the choices of strength and fracture models. In this work, we considered the Geological-Yield Surface (GEO) strength model as our baseline model. However, we did explore

the effects of two other strength models which are discussed later in this report. GEO plasticity model relates the yield strength to pressure as:

$$Y = Y(P) \equiv Y_\infty + (Y_0 - Y_\infty)\exp\left(\frac{P\frac{dY}{dP}\Big|_{P=0}}{Y_0 - Y_\infty}\right), \qquad (7)$$

where Y is the yield strength, $P \geq 0$ is the pressure, Y_∞ is the material yield strength, Y_0 is the yield at zero pressure, and $\frac{dY}{dP}$ (or DYDP, as we will use throughout this work) is the slope of yield surface as a function of pressure at zero pressure. As we describe shortly, DYDP represents the degree of nonlinearity in this strength model. In general, Eq. (7) is valid if $\frac{dY}{dP} > 0$. For cases where $\frac{dY}{dP} < 0$, the following equation is used (again for P≥0):

$$Y = Y(P) \equiv min\left\{Y_\infty, Y_0 + \left|\frac{dY}{dP}\right|_{P=0}\Big|P\right\} \qquad (8)$$

Finally, for $P<0$ (material in tension), GEO model basically reduces to $Y(P) = Y_0$. We note that since pressure is a function of density and temperature, the GEO yield model inherently includes thermal softening and material degradation.

In this work, for all cases, we assumed a value $Y_0 = 10^{-3}$ kbar. Two other input parameters for the GEO model are the Poisson's ratio and melt temperature. For all cases, we assumed the Poisson's ratio to be 0.24 and the material melt temperature to 0.17 eV (~1,973 Kelvins). We note that choices for Poisson's ratio and melt temperature are not based on any specific material. In the literature, there is normally a range of values for Poisson's ratio. For instance, Schultz (1995) reports Poisson's ratio as 0.25±0.05 for intact basalt at ambient temperature of 20 ^{o}C and as 0.3 for basaltic rock mass. In future studies, we plan to explore the effects of Poisson's ratio and melt temperature on seismic response. In this study, to limit the number of parameters and thus simulations, we did not vary Poisson's ratio and melt temperatures. While a more comprehensive uncertainty quantification study requires variations in Y_0, Poisson's ratio, and melt temperature, assuming these three parameters are constants reduces the GEO model to two parameters, namely, DYDP and Y_∞.

Figure 3a shows the effects of degree of nonlinearity, i.e., the slope parameter (DYDP) in the GEO model on the yield as a function of pressure (assuming a yield strength of Y_∞ =1 kbar). Clearly, for DYDP<0, the GEO model is a linear function of pressure and the yield reaches its maximum value at lower pressure values as DYDP decreases. For DYDP>0, the yield strength varies nonlinearly and small DYDP values require higher pressures to achieve yielding of the material (in particular, for DYDP=1). Figure 3b shows yield versus pressure for DYDP=2 and various Y_∞ (noted as Yinf on the plot) values. Naturally, for small Y_∞ values (i.e., weaker material) the material yields at much less pressure compared to larger Y_∞ values (i.e., stronger material) that require much higher pressures to yield the material.

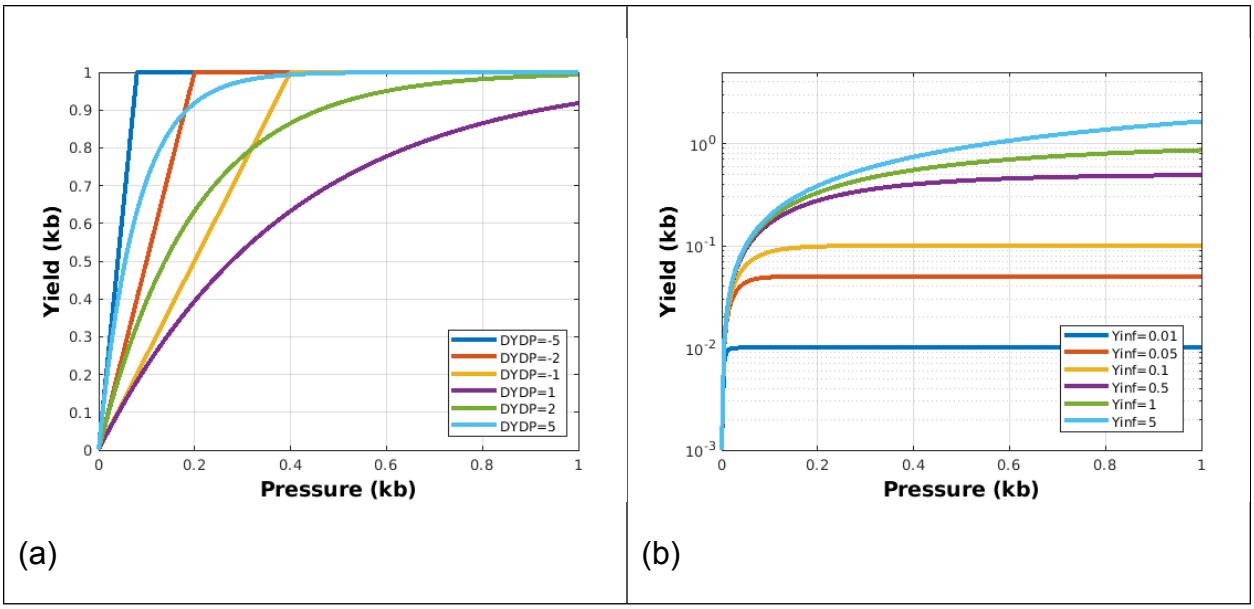

Figure 3. GEO model yield versus pressure: (a) Effects of DYDP parameter and (b) Effects of yield strength, Y_∞ (labeled as Yinf, here) for DYDP=2.

4.3. Other Strength Models Considered

In addition to the GEO model, CTH includes many other "traditional" and "modern" strength and failure models. Many of these models are developed for metals, ceramics, and other materials where there are available experimental data to fit the models. Unfortunately, a lack of model fitting parameters for geologic materials makes it difficult for us to use these more complex models. Here, we explore the effects of two of the "traditional" models. The first model called Elastic Perfect Plasticity, based on von Mises yield surface (EPPVM) model. EPPVM is basically a constant yield surface model. However, CTH tracks the material thermal softening that naturally degrades the material density. The standard inputs required for EPPVM are the yield strength, Poisson's ratio, and material melt temperature [see (Schmitt 2017) for a more detailed discussion].

Another widely used strength model in CTH is the Johnson-Cook strength (flow stress) model, Johnson and Cook (1985).

$$\sigma = \left[A_{JO} + B_{JO}\varepsilon^{NJO}\right]\left[1 + C_{JO} ln\dot{\varepsilon}^{*}\right]\left[1 - T^{*MJO}\right] \qquad (9)$$

Where σ is the flow stress, A_{JO}, B_{JO}, N_{JO}, C_{JO} , and M_{JO} are material dependent constants, ε is the plastic strain, $\dot{\varepsilon}^{*} = \dot{\varepsilon}/\dot{\varepsilon}_0$ is the normalized plastic strain rate with $\dot{\varepsilon}_0 = 1$ (s^{-1}), and $T^{*} = (T - T_{ROOM})/(T_{JO} - T_{ROOM})$ is referred to as the homologous temperature with T_{ROOM} being the room (ambient) temperature and T_{JO} is the material melt temperature. We note that σ, A_{JO}, and B_{JO} have units of pressure (i.e., dynes/cm^2 in terms of CTH units), N_{JO}, C_{JO} , and M_{JO} are dimensionless parameters, and temperatures T, T_{ROOM} and T_{JO} are in (eV). We kept the subscripts *JO* to be consistent with the convection used in CTH documentation [see (Schmitt 2017)]. There is a lack of data in the literature for Johnson-Cook strength models parameter.

Therefore, in this work, we treat A_{JO}, B_{JO}, N_{JO}, C_{JO}, and M_{JO} parametrically, using a small set of values. We should note that Johnson-Cook strength model also includes its own damage model that is based on a cumulative strain:

$$D = \sum \frac{\Delta\varepsilon}{\varepsilon^f} \tag{10}$$

where D is the cumulative damage, the summation is over time, $\Delta\varepsilon$ is the increment (in time) of the equivalent plastic strain, and ε^f is the equivalent strain to fracture Johnson and Cook (1985) and is given as:

$$\varepsilon^f = [D_1 + D_2 e^{D_3\sigma^*}][1 + D_4 ln\dot{\varepsilon}^*][1 + D_5 T^*] \tag{11}$$

where D_1 to D_5 are five additional material dependent parameters for the damage model, $\sigma^* = \sigma_m/\bar{\sigma}$ is the ratio of the average three normal stresses (in three-dimensions) and $\bar{\sigma}$ is the von Mises equivalent stress. In this model damage begins when D becomes non-zero and material fracture occurs when D=1.0.

To reduce (and thus limit) the number of model parameters for Johnson-Cook strength and damage models , in this work, we assumed M_{JO}=1, and choose D_1 to D_5 such that $\varepsilon^f \sim 1$ (D_1=D_2=1/2, D_3=-10, D_4=D_5=0). That is, damage is primarily computed as the integral of the change in equivalent plastic strain over time. We note that our selection of D_1 to D_5 is mainly to reduce the number of parameters in our analyses. We plan to explore the effects of D_1 to D_5 parameters on damage in a future study.

5. SIMULATION RESULTS

We note that in Subsections 5.1*5.5*, we use COMP-C4 as the explosive material for all simulations. However, in Subsection 5.6 and subsequent sections, we will use COMP-B as the explosive charge for our simulations. While programmatically, COMP-B is the explosive of choice, we initially used COPM-C4 to perform our baseline simulations. We will use COMP-B for all future works.

5.1. Baseline GEO Model Results

we examine the effects of Y_∞ and DYDP in the GEO model on the resulting RDPs for our baseline problem. To set the stage, we first discuss CTH simulation results and typical RDPs, for a case where DYDP = 2 and $Y_\infty = 0.05$ kb. With respect to material fracture, the GEO model does not include an explicit damage model. The standard fracture model is based on a user-defined tensile or fracture pressure values. For simplicity, we set fracture pressure, $P_{frac} = -Y_\infty$ for all cases. We have performed a limited study of varying P_{frac}, which we will discuss later.

As an example of CTH results, Figure 4 shows the material pressure (top left), velocity magnitude (top right), J2P (lower left; see explanation below) and yield strength (lower right) at *t*=0.5 sec, for the entire computational domain. The stratification in pressure field is the result of the gravitationally stable option in CTH. The velocity magnitude field clearly illustrates the shock front has travelled nearly 2 km downward and has reached the top and side boundary—as evident by the spherical shock waves, reflections from the side and the interaction with the atmosphere above the rock surface. The bottom panel of Figure 4 include the J2P (J2 plasticity) and the GEO yield fields. In two-dimensions (i.e., the simulations in this work), J2P is simply the general plane stress representation of von Mises stress

$$\sigma_{vm} = \sqrt{\sigma_{11}^2 - \sigma_{11}\sigma_{22} + \sigma_{22}^2 + 3\sigma_{12}^2} \quad (12)$$

where $\sigma_{vm}$is the von Mises stress, $\sigma_{11}$and σ_{22} are the XX (subscript 11) and YY (subscripts 22) deviatoric stresses and σ_{12} is the shear stress in XY direction.

In CTH, plasticity is achieved when, $\sigma_{vm} > Y$. As the left panel of Figure 4b shows, as expected, the largest J2P values are near the explosion (i.e., around the DOB) and the high values are in the 15-30 bar range (i.e., below the yield strength value of 0.05 kb used in this example) and thus no plastic flow occurs. The highest J2P value of ~0.044 kb is confined to a zone near the cavity. The GEO model yield (in the right panel of Figure 4b) shows that the yielded (i.e., 5E7 dynes/cm^2=0.05 kb) wet tuff zone (fully red) extends to the edge of the shock front. Near the surface there is a layer that shows yield values below 0.05 kb. Naturally, since the pressure increases as the depth increases, the material tends to experience yielding near the surface, unless the yield strength is much higher.

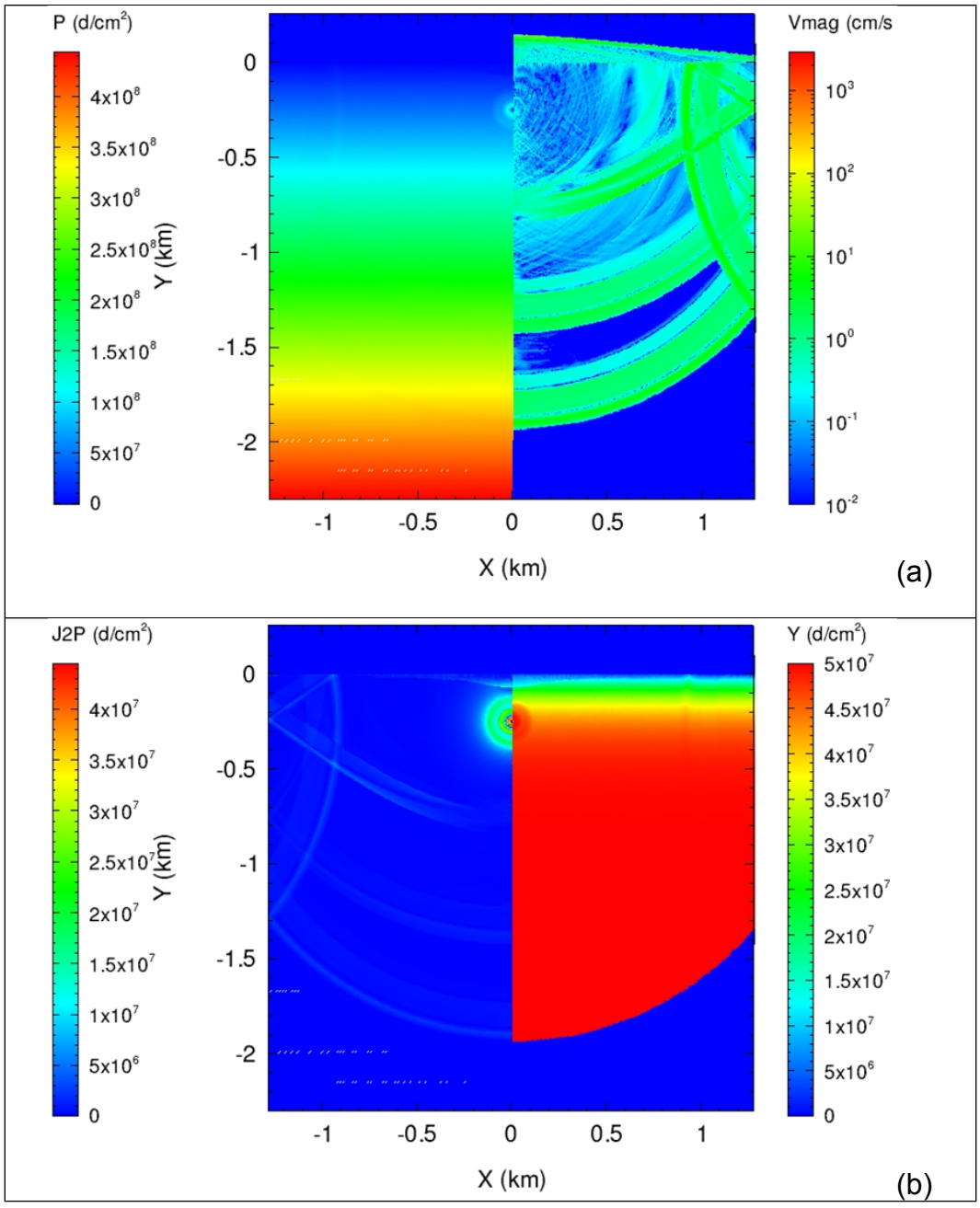

Figure 4. Full domain views of CTH results for the baseline case at 0.5 sec.: (a) material pressure on the top left panel and velocity magnitude on the top right panel; (b) J2P on the bottom left panel and yield on the lower right panel.

Figure 4 shows the close-up (i.e., near and around the DOB) views of the density field (left) and resulting cavity (right, white circle) for a COMP-C4 detonation, at t=0.51 sec. The blue color in the density plot (~0.001 g/cc) is the low-density explosive gases that are trapped in the cavity and the red is the rock density of ~1.97 g/cc. The cavity, which is 8.17 m in radius, is the result of the movement shock generated by the high-pressure, high-velocity explosive gases. We note that the change in cavity radius should be calculated as the final cavity radius, $R_{cav,f}$ (8.17 m,

here) minus the original cavity radius for the high explosive, R_{HE} (~1.39 m, in this case). Therefore, we find the resulting final cavity radius as:

$$R_{cav}=R_{cav,f}-R_{HE}$$

to be ~5.92 m or a scaled cavity size of $R_{s,cav}$ ~22.6 m/kt$^{1/3}$. It is important to bear in mind that here we are assuming perfectly homogenous rock without cracks and/or heterogeneities. Also, we are not allowing for the explosive gases to vent out into the atmosphere. Therefore, the resulting cavity might differ from what is shown here. With respect to how the (gas-filled) cavity is formed, we examined the changes in material temperature to see if there was any rock melting. We found in most cases; the maximum temperature of geologic material was ~560 K, relatively early (within the first 0.1 sec) in the simulations. We think that in the case of the chemical explosions simulated in this study, that the cavity is formed primarily due to the high pressure, high velocity gas compressing the ground outward and not ground material phase change.

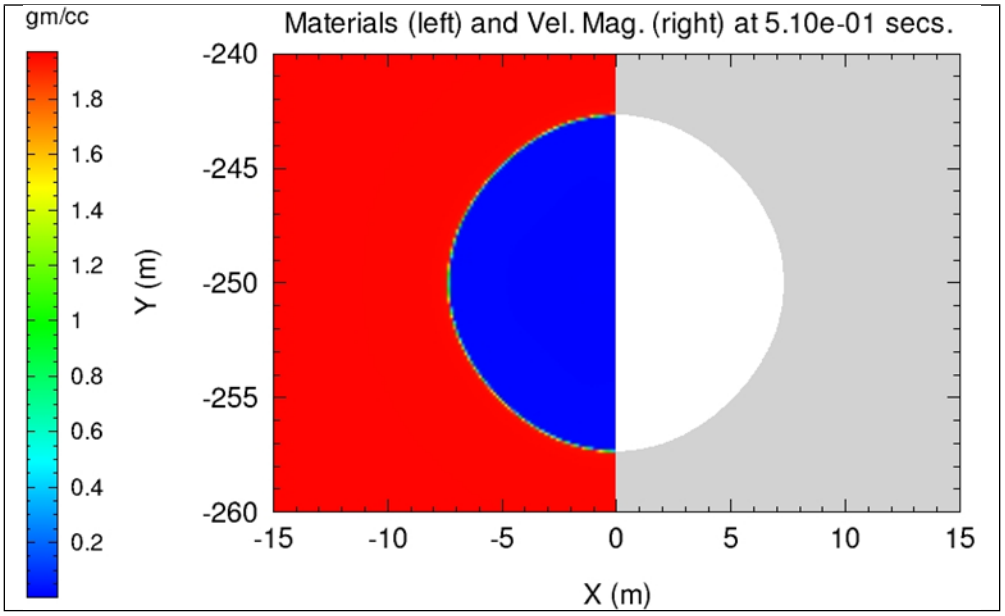

Figure 5. Close-up view of the cavity formed by explosion of 18 t of COMP-C4 in a tamped environment: Left panel density field and right panel resulting cavity (white) and the grey background is wet tuff.

Now we return to how the CTH results are converted to RDP histories. The RDP code reads in the data for a series of stationary (fixed and/or Eulerian) tracers, placed radially outward along y=-250 m (DOB). Figure 6 depicts typical RDP plots for various tracer points. There is generally a rise in RDP until it reaches a maximum value after which it drops and eventually settles to a value. As we go farther out (i.e., away from the explosion) where the ground response is supposed to be elastic, the RDPs tend to converge. For instance, in this figure, there appears to be a convergence from roughly 290 m and beyond. Another interesting feature of the "converged" RDP curves is the presence of several inflection points, namely, the initial peak, followed by a short time flattening and then a drop to a local minimum and then rises again, before settling into a nearly steady value. The local minimum is an artifact since the RDP

calculation does not account for free surface effects. Recall from Eq. (3) that RDP is a function of time integral of a product of an exponential term and the radial displacement history.

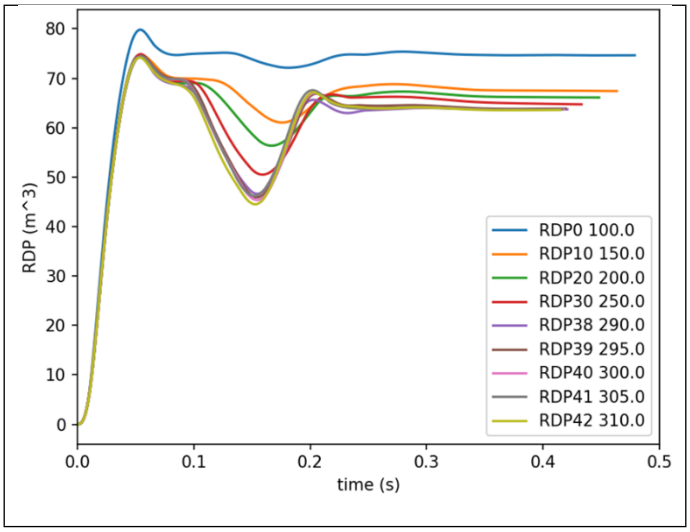

Figure 6. RDP versus time curves for various tracer points, for the baseline problem. The numbers in the legend are tracer numbers followed by the tracer location in meters.

Figure 7 shows the radial displacement histories used to generate the RDPs in Figure 6. We can see from Figure 7 peak displacement diminishes for the tracers farther away from the explosion. We also see several tracers show nearly identical histories (i.e., for the RDPs we called as "converged") with peak displacement value of ~0.3 cm. While the various inflection points do not directly relate to the oscillations in radial displacement curves, we see that the displacement does vary enough that its contribution to the integral term results in a complex looking RDP curve. In fact, we found that the valley (i.e., the drop to a minimum in RDP) is generally the result of low frequency, sort amplitude oscillations in the radial displacement history (e.g., before 0.2 and 0.3 sec in this figure). We note that we do not perform any filtering of our simulation (i.e., CTH) results, when we generate the corresponding RDPs. We assume a low pass filter might remove some of these oscillations—something that we will examine in a future study. Moreover, these oscillations are also present as a result of the interaction of the wave reflections from the surface (i.e., the air-rock interface).

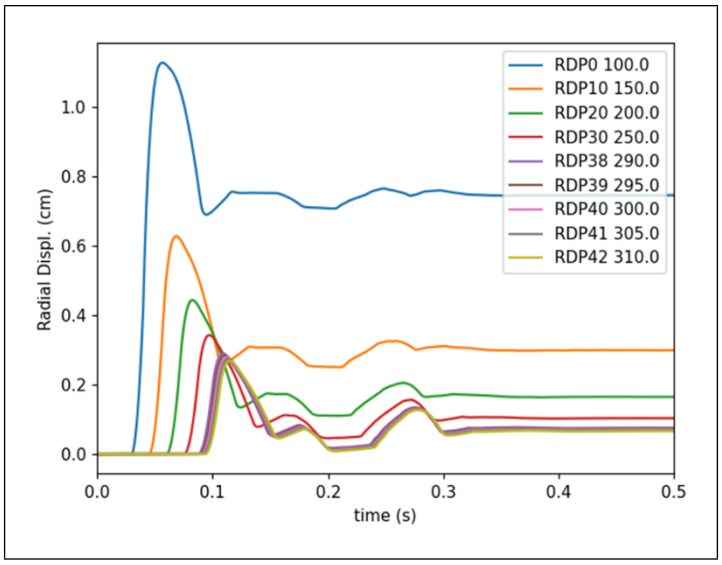

Figure 7. Radial displacement versus time curves for various tracer points, for the baseline problem. The numbers in the legend are tracer numbers followed by the tracer location in meters.

Figure 8 shows the peak RDP and radial distance versus scaled radial distance (where the radial distance is based on the tracer locations. The peak radial displacement has a nearly 1/r response. Although as the "true" elastic radius is approached peak RDP should settle to a steady value, we see small variations in the peak RDP. These variations are a direct result of variation in the radial displacement history, possibly arising from reflections from the surface (or the right boundary). This is one of the limitations of the RDP model, since it does not consider surface and other complex effects that are prevalent in nonlinear source models.

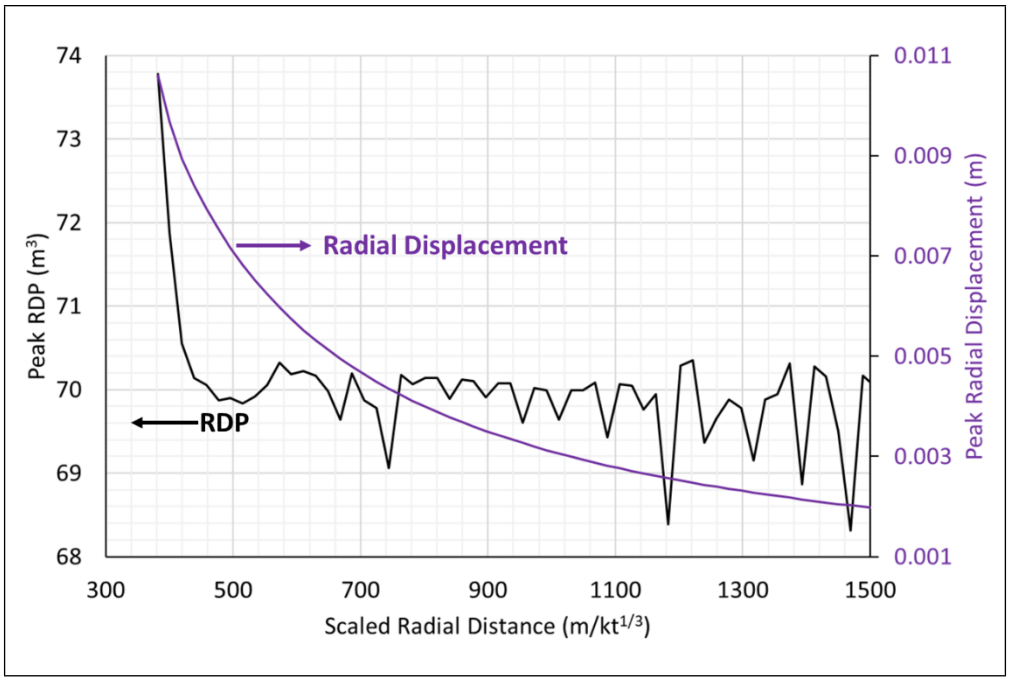

Figure 8. Peak RDP (left ordinate axis) and peak radial displacement (right ordinate axis) versus scaled radial distance for the baseline GEO model being discussed here. Although we see small variation in peak RDP (after ~500 m/kt$^{1/3}$, on average the peak RDP is ~70 m^3. The small variations in RDP are a direct result of variation in the radial displacement history. The peak radial displacement shows an expected ~1/r (r being the radial direction) response.

Figure 9a shows the trends in the GEO yield histories for the various tracers presented in the previous two figure and Figure 9b includes the pressure histories. Both yield and pressure curves depict the same clustering (convergence) for the converged RDPs. Moreover, the peak yield and pressure values drop as the tracer distance increases. Another observation is that the peak yield never reaches its maximum value of 0.05 kb for these tracer points. This is consistent with the low yield stress region near the air-rock interface in Figure 9b.

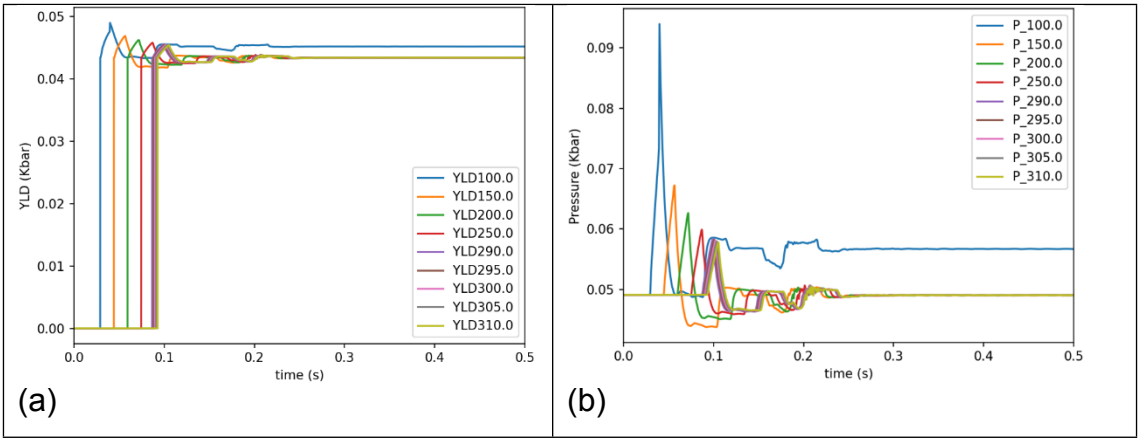

Figure 9. (a) GEO yield and (b) pressure time histories for various tracer points, for the baseline problem. The numbers in the legend are the tracer location in meters.

5.2. A Note of the Effects of Fracture Pressure

Here, we provide a short discussion of the effects of fracture pressure, P_{frac}. Figure 10 depicts the calculated RDP time histories for a tracer at radius of 300 m, using P_{frac}=-0.025 kb, -0.05 kb (our baseline value), and -0.1 kb. In general, we see little differences in the RDP peak value as a function of the P_{frac}. However, there are small differences in the minimum and second peak. It also appears that the three RDPs eventually reach nearly the same steady value around 0.4 sec. We again note that the minimum (i.e., the valley) and the second smaller peaks are likely artifacts of the RDP calculations (i.e., small oscillations in the radial displacement history that can affect the RDP signal).

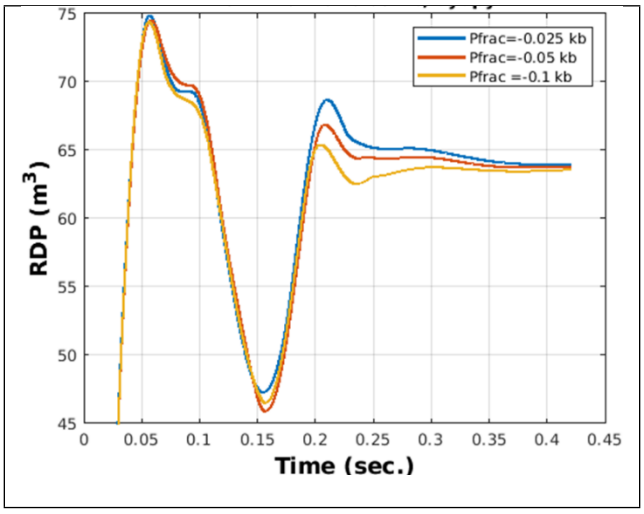

Figure 10. Close-up view of the RDPs tracer at of 300 m, using three different fracture pressure values for the baseline problem.

In Table 3. Peak RDP, radial velocity, and radial displacement along with final scaled cavity radius for three different fracture pressure values., we list the peak RDP, radial velocity, and radial displacement values at radius of 300 m, along with the scaled cavity radius at the end of the simulation. This list, which is a convenient way of quantifying a few key results, shows that the choice of P_{frac} (for the range of values used here) has little effect on the peak values as well as the final cavity size.

Table 3. Peak RDP, radial velocity, and radial displacement along with final scaled cavity radius for three different fracture pressure values.

P_{frac} (kb)	Peak RDP (m^3)	Peak Radial Velocity (m/s)	Peak Radial Displacement (m)	Cavity Scaled Radius ($m/kt^{1/3}$)
-0.025	74.4	0.27	0.0028	22.6
-0.05	74.3	0.27	0.0028	22.6
-0.1	74.3	0.27	0.0028	22.6

5.3. Effects of Mesh Resolution

In CTH the AMR resolution level is controlled using the "MAXL" parameter. For our baseline simulations that use a 12.5 cm mesh spacing, MAXL=10. Each MAXL changes the mesh size by a factor of two. Here, we consider two other mesh sizes, 6.25 cm (MAXL=11) and 25 cm (MAXL=9). To illustrate the effects of mesh resolution on the RDP, Figure 11 shows the close-up view of the RDP history at the 300 m range (as we have used for other cases being discussed here). The general observation is that mesh resolution has little effect on the overall response of the RDP, especially for the peak and minimum values, between our baseline resolution of 12.5 cm and 6.25 cm. However, there are small differences as the RDP reaches a steady response, later in time.

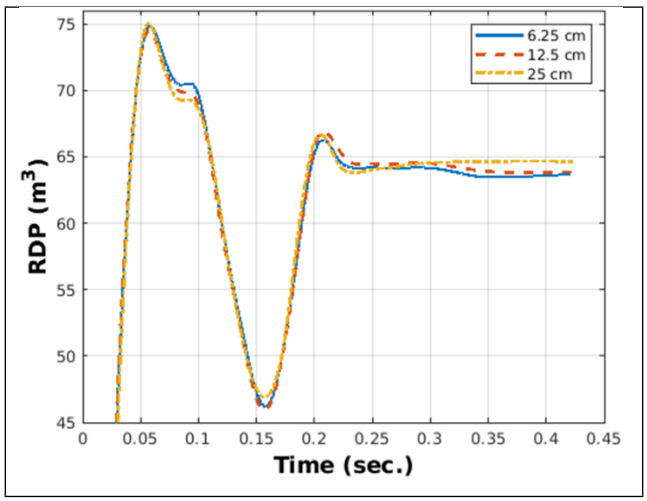

Figure 11. Close-up view of the RDPs tracers at of 300 m, using three different mesh resolutions for the baseline problem.

Table 4 lists the values for the peak RDP, radial velocity, and radial displacement (at the 300 m range) along with the scaled cavity radius for the different mesh resolutions. The key take-away from the list is that coarser resolutions, which by nature introduce additional numerical diffusion, tend to result in a slightly larger final cavity. However, the differences are not large enough for our discussion here and for the remainder of this report, we used a 12.5 cm resolution. Yet, we know that choice of mesh resolution is a major source of uncertainty in quantifying seismic response to underground explosions. We also do not claim that we have reached a so-called "converged" solution, as we need to resolve the problem with at least one other AMR level (i.e., 3.125 cm cell resolution).

Table 4. Peak RDP, radial velocity, and radial displacement along with final scaled cavity radius for three different mesh resolutions.

Mesh Resolution (cm)	Peak RDP (m^3)	Peak Radial Velocity (m/s)	Peak Radial Displacement (m)	Cavity Scaled Radius ($m/kt^{1/3}$)
6.25	74.9	0.28	0.0028	22.5
12.5	74.3	0.27	0.0028	22.6
25	74.2	0.27	0.0028	22.8

5.4. Effects of Yield Strength in GEO Model

To examine the effects of yield strength, Y_∞, in the GEO strength model, we chose six yield strength values, namely, 0.01, 0.05, 0.1, 0.5, 1, and 5 kb to mimic materials ranging from weak to very strong. For all cases, we set DYDP=2. Figure 12a shows the RDP histories (at range of 300 m) for Y_∞=0.01, 0.05, and 0.1 kb (Yinf in the figure's legend). Figure 12b shows the RDPs for the 0.5, 1, and 5 kb Y_∞ values, where the RDPs for 0.5 and 1 kb cases are at a range of 170 m and for the 5 kb at a range of 155 m. We notice as the yield strength increases the RDP becomes more depressed and shows progressively smaller values. The peak RDP for the 0.01 kb case is ~2.6 times larger than that of 0.05 kb (our baseline case) and the minimum following the peak is slightly later in time for the 0.01 kb case than that of 0.05 kb, which is a direct effect of the behavior of the radial velocity and thus radial displacement over time. For larger Y_∞ values the RDPs are below 20 m^3. In general, cases with larger yield strength tend to converge closer to the source. That is why in Figure 12b we chose a different range/location for the RDPs.

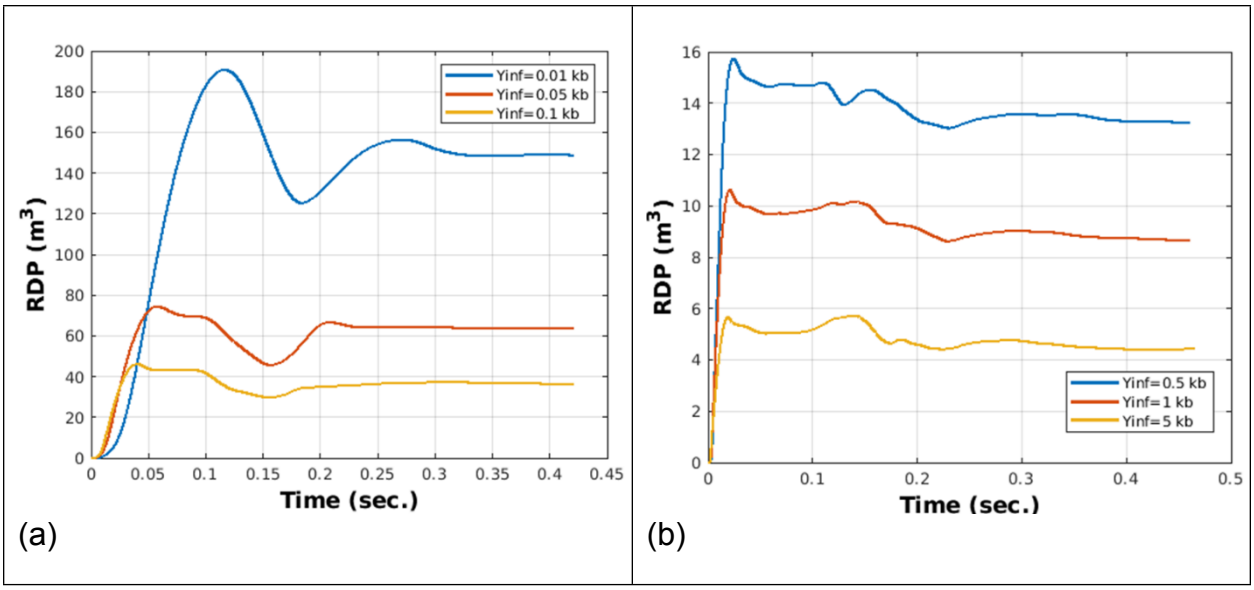

Figure 12. RDPs for six different yield strength values of the GEO model for our baseline case using DYDP=2: (a) RDPs for the 0.01, 0.05, and 0.1 kb yields strength for tracers at 300 m range and (b) RDPs for 0.5 and 1 kb yield strength values for tracers at 170 m range and for 5 kb yield strength at 155 m range. We noticed that for larger yield strength (i.e., 0.5 kb and above), the RDPs tend to converge closer to the source than the lower yield strengths. That is why we chose different radial distances for RDPs in frame (b).

From our simulations, we noticed as the material gets stronger the resulting cavity formed is progressively smaller (see Figure 13). This is not a surprising result, since as the material strength increases, for the same explosive source, a smaller region of the ground material near the explosion tends to undergo deformation and fracture. From the figure, we also see that for the higher strength cases ($Y_{\infty} \geq 0.5$ kb), the cavity formation happens much earlier and there is generally a rise to maximum, after which the cavity size does not vary. For the lower strength cases, on the other hand, there appears to be a gradual rise to a maximum cavity size and then there is a small drop (likely due to relaxation) before the cavity size stabilizes.

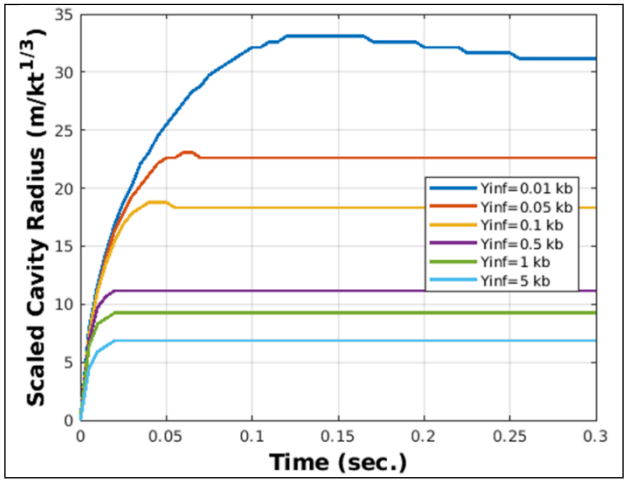

Figure 13. Scaled cavity size versus time as a function of yield strength in GEO model and DYDP=2 shows the final cavity size decreases as the yield strength (Y_∞) increases.

Finally, the peak values that we have been listing for the various runs, are included in Table 5. Again, the peak values are at a 300 m range and the scaled cavity radius represents the value at the end of simulation (i.e., 0.5 sec.). Generally, the yield strength increases as the peak RDP decreases (and of course, so does the cavity size). On the other hand, increasing yield strength increases the peak radial velocity and displacement.

Table 5. Peak RDP, radial velocity, and radial displacement along with final scaled cavity radius for six different yield strength (Y_∞) values of GEO model.

Yield Strength (kb)	Peak RDP (m^3)	Peak Radial Velocity (m/s)	Peak Radial Displacement (m)	Cavity Scaled Radius ($m/kt^{1/3}$)
0.01	189.9	0.15	0.004	31.2
0.05	74.3	0.27	0.0028	22.6
0.1	45.7	0.35	0.0023	18.3
0.5	15.5	0.57	0.0014	11.1
1	10.5	0.67	0.0011	9.2
5	5.6	0.79	0.0008	6.9

5.5. Effects of the Slope Parameter (DYDP) in GEO Model

Next, we examine the effects of the slope parameter (DYDP) in the GEO model on the RDP response. Here, we decided to use the lowest strength case discussed in Section 5.4 (i.e., Y_∞ =0.01 kb and let $P_{frac} = -Y_\infty$=-0.01 kb and all other problem parameters are same as before). Our motivation for choosing Y_∞=0.01 kb was to ensure that the RDP is well-behaved and

converges at 300 m range. Additionally, at a lower yield strength, the material tends to yield (i.e., reach maximum yield strength) thus allowing us to observe the wave response under the material yield conditions. We will repeat these simulations for the higher yield strength cases in the future. Figure 14 compares the close-up view of the RDPs for six different DYDP values. In general, the RDP histories show little difference for various DYDP values, except for DYDP=1. For DYDP=1, the RDP has a slightly higher peak than other cases, displays a higher minimum than other cases, and finally rises and reaches a near steady RDP value that is lower than the other cases. Recall from Figure 3a that for DYDP=1, the GEO model shows a slow rise from zero yield and reaches full yield strength at much higher pressures than all other DYDP values (whether negative and/or positive). Nevertheless, it appears that, in general, the DYDP parameter does not greatly affect the response of RDP. More likely, we need to spot check this behavior, specifically the DYDP=1 case for other yield strength values.

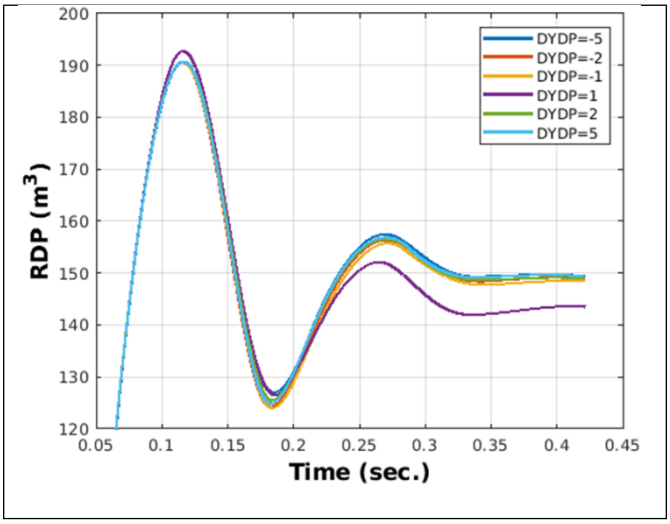

Figure 14. Close-up view of the RDPs for a tracer at 300 m range showing the effects of the DYDP (slope) parameter in the GEO model, using a yield strength of 0.01 kb. The RDPs are nearly identical for all DYDP values, except DYDP=1, which shows higher peak and reaches steady state at a lower RPD than all other cases.

In Table 6, we list the peak RDP, radial velocity, and radial displacement (all at a range of 300 m) and the cavity scaled radius at 0.5 sec for different DYDP values. As we saw in Figure 14, DYDP=1 shows the highest RDP peak, as listed below, and the variations in peak RDP among the other cases in negligible. Yet, the peak radial velocity and displacement seem to be unaffected by the choice of DYDP. The scaled radius for the final cavity is also the same, but again DYDP=1 shows a smaller cavity size than the other cases. Our experience with the GEO model, thus far, generally indicates that higher peak RDPs result in larger cavities. However, this is not the case for DYDP=1, where a larger peak RDP does not necessarily mean larger cavity formation. To better understand if DYDP~1 is appropriate to use for our applications, we need to perform simulations against actual experimental data.

Table 6. Peak RDP, radial velocity, and radial displacement along with final scaled cavity radius for six different slope parameter (DYDP) values of GEO model.

DYDP (-)	Peak RDP (m^3)	Peak Radial Velocity (m/s)	Peak Radial Displacement (m)	Cavity Scaled Radius ($m/kt^{1/3}$)
-5	190.3	0.15	0.004	31.2
-2	190.5	0.15	0.004	31.2
-1	190.4	0.15	0.004	31.2
1	191.4	0.15	0.004	30.7
2	189.9	0.15	0.004	31.2
5	190.26	0.15	0.004	31.2

5.6. Effects of Explosive Material

Up to this point, we have used COMP-C4 as the explosive charge. Next, we explore the effects of using COMP-B on the RDP response. As a reminder, Table 2 lists the properties as well as the JWL parameters for COMP-B used in our study. We note that COMP-B is slightly denser than COMP-C4 and has slower detonation velocity (D_{CJ}). As before, we model the explosive as a sphere, which in the case of COMP-B has a radius of 135.76 cm (for an 18-ton TNT equivalent charge). For this case, we went back to our baseline parameter values for the GEO model, i.e., Y_∞=0.05 kb, DYDP=2, P_{frac}=-0.05 kb and the mesh resolution was also 12.5 cm. Figure 15. Comparison of RDP using COMP-C4 to that of COMP-B for a tracer at 300 m range. Both cases are based on the GEO strength model with 0.05 kb yield strength.
 shows a comparison of the RDPs for COMP-C4 and COMP-B. The RDP for the COMP-B case generally is smaller than that of COMP-C4. The shape of the two curves is nearly identical, except that the COMP-B RDPs are slightly lower (generally, 5-6%). Overall, however, COMP-B and COMP-C4 have similar responses.

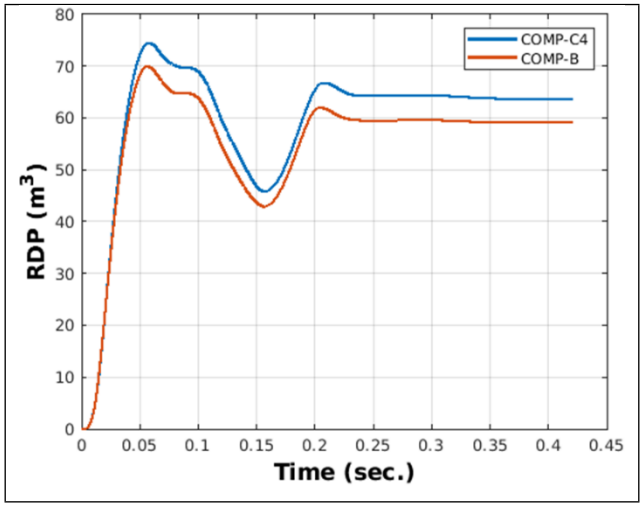

Figure 15. Comparison of RDP using COMP-C4 to that of COMP-B for a tracer at 300 m range. Both cases are based on the GEO strength model with 0.05 kb yield strength.

In Table 7, we list the peak RDP, radial velocity, and displacement at 300 m range and, as before the cavity size at the end of the simulation. It is interesting that overall, the peak radial velocity and displacement are nearly the same for the two explosives, even though the peak RDPs are different. We also see that COMP-B results in a slightly smaller cavity than COMP-C4. Again, as we have seen with other cases, a lower peak RDP generally indicates a smaller cavity radius.

Table 7. Peak RDP, radial velocity, and radial displacement along with final scaled cavity radius for two different high-explosive materials.

Explosive Material	Peak RDP (m^3)	Peak Radial Velocity (m/s)	Peak Radial Displacement (m)	Cavity Scaled Radius ($m/kt^{1/3}$)
COMP-C4	74.3	0.27	0.0028	22.6
COMP-B	69.8	0.27	0.0026	22.2

5.7. Effects of Other Strength Models

Table 8 lists the parameter values we used for six different simulations, JC1-JC6, using the Johnson-Cook model. Note, here we interpret the constant A_{JO}, in the Johnson-Cook model as the yield strength parameter.

Table 8. Johnson-Cook strength model parameters used for six different cases studied in this work.

Case	A_{JO} (kbar)	B_{JO} (kbar)	N_{JO} (-)	C_{JO} (-)	M_{JO} (-)
JC1	0.05	0.0	0.0	0.0	1
JC2	0.05	0.01	0.25	0.0	1
JC3	0.05	0.05	0.25	0.0	1
JC4	0.05	0.1	0.25	0.0	1
JC5	0.05	0.0	0.0	0.01	1
JC6	0.05	0.05	0.25	0.01	1

We first compare the GEO model (i.e., the result shown in Figure 15) to a case using EPPVM and JC1 listed in the table above. The yield strength for the EPPV and JC1 are the same as in the GEO model, i.e., 0.05 kb. We note that we will use COMP-B as the high-explosive charge for the rest of the report. The choice of parameters for JC1 reduces Eq. (10) to a linear model that varies with temperature. Figure 16 compares the RDP for the three models at a range of 300 m. Clearly, the GEO model shows a higher peak RDP than the other two models. While all three models converge at the same value of ~60 m^3, the differences in the RDP shapes are likely an artifact of the differences in the radial displacement history among the three models.

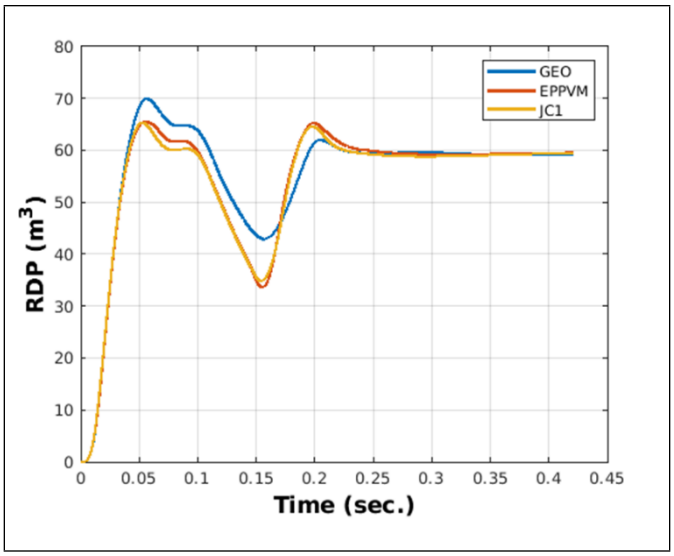

Figure 16. RDP versus time for a tracer at 300 m range, using GEO, EPPVM, and linearized Johnson-Cook models. For these cases, the explosive source is COMP-B and the yield strength for all cases is 0.05 kb.

To better understand the differences and similarities among these results, Figure 17 compares the yield history, at 300 m, for the three strength models. While all three models have the same rise time, the GEO model shows a maximum value slightly above 0.045 kb (i.e., never reaches the 0.05 kb yield strength value) and then drops with variations that eventually reach a steady value. The EPPVM and JC1, on the other hand, have a step-function like rise to the maximum value of 0.05 kb (i.e., the input yield strength). Since the EPPVM is a constant strength model, and at this location the material does not undergo thermal softening and/or density degradation, the input yield strength is the only value at that location. A similar situation also true for the JC1 model. Based on our parameter choices for JC1, at the 300 m radial location the ground temperature is nearly at ambient temperature, thus making the T^* term in Eq. (10) nearly zero, resulting in strength (or flow stress) value that is equal to A_{JO}=0.05 kb. Since EPPVM and JC1 reach the yield strength limit and GEO does not, the GEO material behaves as a weaker material than EPPVM and JC1. Based on our earlier observation that we generally see a higher peak RDP for weaker materials than those of stronger materials, there is an inconsistency between the RDP response in Figure 16 and the material strength response in Figure 17. That is, the model that shows "full yielding" would be expected to behave like a weaker material. Given the complexities of nonlinear strength/stress models, to better understand these differences, more likely, we need to process these results using AxiElasti code, Preston (2017).

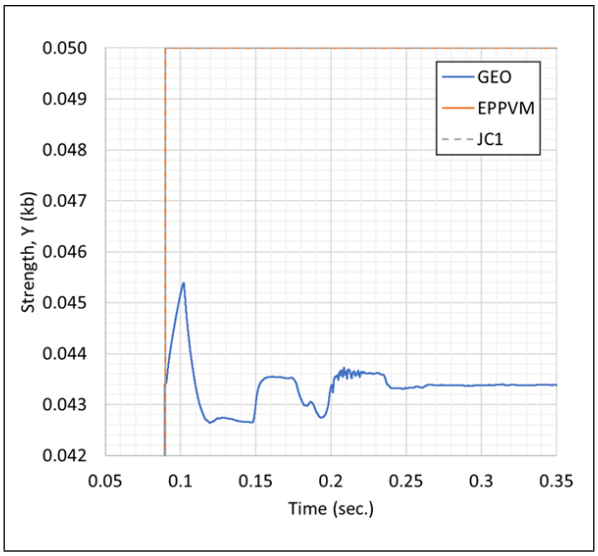

Figure 17. Material strength versus time at the 300 m tracer location for three different strength models. For all models the yield strength of wet tuff (ground material) is set to 0.05 kb.

In Table 9, we summarize the key peak values and the cavity sizes for our three cases. We discussed the peak RDPs in the previous paragraph. Also, based on our explanations of the strength response, above, we see that the GEO model (i.e., apparently weaker material) results in a larger cavity at the end of the simulation than the cavities formed by the EPPVM and JC1 models.

Table 9. Peak RDP, radial velocity, and radial displacement along with final scaled cavity radius for three different material strength models available in CTH.

Strength Model	Peak RDP (m^3)	Peak Radial Velocity (m/s)	Peak Radial Displacement (m)	Cavity Scaled Radius ($m/kt^{1/3}$)
GEO	69.8	0.27	0.0026	22.2
EPPVM	65.9	0.27	0.0026	21.3
JC1	66.9	0.27	0.0026	21.3

5.8. Effects of Johnson-Cook Parameters

We now discuss the results for the other Johnson-Cook (JC) cases (i.e., JC2-JC6) listed in Table 8 and how these parameters affect the RDPs. Except for the parameters listed for JC2-JC6, we did not alter any other parameters for the simulations and continue to use COMP-B as the explosive charge. Figure 18 shows the converged RDP histories, for six different variations of the JC strength model. We previously showed the JC1 result, when comparing a linearized version of the JC strength model to GEO and EPPVM model in Figure 17. JC2, JC3, and JC4 cases explore the effects of equivalent strain on the RDP, where we increase B_{JO} and thus the

equivalent strain term effects. Increasing B_{JO} (as displayed in Figure 18) has noticeable effects on the RDP, which clearly results in smaller RDP values. In other words, as $B_{JO,}$ and thus the effects of equivalent strain increase, the ground material acts more rigid (i.e., stronger). The JC5 case includes a non-zero C_{JO} value that activates the effect of strain rate in the model. Since away from the explosive the strain rate in ground material is small (i.e., the assumption of near elastic response), JC1 and JC5 RDP responses are relatively similar, although, we see differences between JC1 and JC5 around 0.2 sec. This difference is likely because JC5 includes the effect of strain rate that is not present in JC1. Finally, JC6 parameters are same as JC3 except for the addition of C_{JO}=0.01 (i.e., as in JC5 includes the strain rate effects). The RDP curve for JC6 shows a response that is like that of JC3. That is likely because, again, the equivalent strain rate is too small (or nearly zero) at that location to affect the strength, or the equivalent strain is more dominant than that of the strain rate. The key take-away from these results is B_{JO} seems to have the most prominent effect on the RDP response and likely the seismic response. In addition, given that variations in JC strength model parameters do yield different results, we might need to perform a more comprehensive study of this model, especially for different subsurface materials, and especially where experimental data might be available. Finally, we note that, based on these parameter values, the cumulative damage was always less than 1.0 (i.e., based on these parameter values, we did not observe any material damage resulting from the JC model).

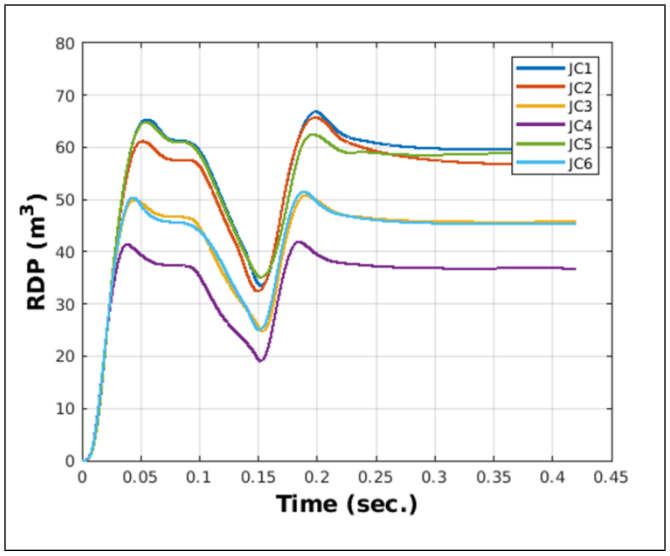

Figure 18. RDP versus time for a tracer at 300 m range, for Johnson-Cook (JC) model. Each case, JC1-JC6 represent variation of one of the parameters in the JC strength model.

Table 10 summarizes the peak RDP, radial velocity, and radial displacement values for JC1-JC6 cases discussed here. The table also includes the final scaled cavity at the end of the simulations. Additionally, we have included the various parameter values (previously listed in Table 8) to see the effects of each parameters more clearly on the results. In general, we do not see variations in the peak radial velocity and displacement values. As we have seen so far, we also see a direct correlation between the peak RDP and cavity size. That is, the smaller the peak RDP, the smaller the resulting cavity and *vice versa*. The lack of variations in peak radial velocity (or displacement) indicates that it is the shape of the velocity/displacement waveform that affects the final RDP.

Table 10. Peak RDP, radial velocity, and radial displacement along with final scaled cavity radius for the six different cases using the Johnson-Cook strength model.

Case	A_{JO} (kbar)	B_{JO} (kbar)	N_{JO} (-)	C_{JO} (-)	M_{JO} (-)	Peak RDP (m^3)	Peak Radial Velocity (m/s)	Peak Radial Displacement (m)	Cavity Scaled Radius ($m/kt^{1/3}$)
JC1	0.05	0.0	0.0	0.0	1	66.9	0.27	0.0026	21.3
JC2	0.05	0.01	0.25	0.0	1	61.9	0.27	0.0026	20.8
JC3	0.05	0.05	0.25	0.0	1	50.9	0.28	0.0024	18.9
JC4	0.05	0.1	0.25	0.0	1	42.0	0.29	0.0022	17.0
JC5	0.05	0.0	0.0	0.01	1	64.9	0.26	0.0026	21.3
JC6	0.05	0.05	0.25	0.01	1	51.6	0.27	0.0024	18.9

6. EFFECTS OF GEOLOGIC MATERIALS

We performed another set of simulations where we considered three other ground materials, basalt (SESLAN #7530, ρ_0=2.87 g/cc), salt (SESLAN #7282, ρ_0=2.14 g/cc), and dry tuff (ANEOS #7122, ρ_0=1.83 g/cc), where ρ_0 is the initial density, in comparison to the baseline of wet tuff (SESLAN #7120, ρ_0=1.95 g/cc). For these cases, we used the GEO strength model for a yield strength of 0.05 kb and the explosive charge was COMP-B. We realize that these materials (as well as our baseline material wet tuff) have different yield strengths, fracture, and other material responses. However, here for ease and consistency, we use the same material response model for all cases and purely examine the effects of material through the choice of EOS on the RDP response. Figure 19 compares the RDPs, at 300 m range, for the four different ground materials. Among all the materials examined here, dry tuff has the lowest and basalt has the highest initial density. The basalt RDP has the lowest first peak compared to other materials. However, the late time response of the basalt RDP (~0.3 sec. and later) is unusual, that is, the drop around 0.27 second and formation of a second minimum. Clearly, we do not see that for the other materials. We examined the RDPs for basalt at other tracer locations as well and saw the same behavior. Since we can generally trace the RDP response back to the radial velocity, we examined these and noticed there is a period from ~0.2-0.3 where the velocity is zero. However, after 0.3 sec., reflections from the right boundary result in velocities ranging from -0.05 to +0.04 m/sec, thus resulting in non-zero late time radial displacements; thus, we interpret the late-time drop in the basalt RDP as an artifact from numerical domain boundary reflections and not due to a physical cause. Extending the right boundary farther out does not greatly add to the computational burden. In the future, we will examine the effects of a large computational domain on basalt's response. Salt and dry tuff have nearly the same first RDP peak, with wet tuff having the largest peak among the four materials. Clearly, the choice of ground material (EOS) has profound effects on the RDP and likely in the resulting seismic signals. However, we need to keep in mind that here, we are merely looking at the differences due the EOS and not necessarily the strength and fracture models.

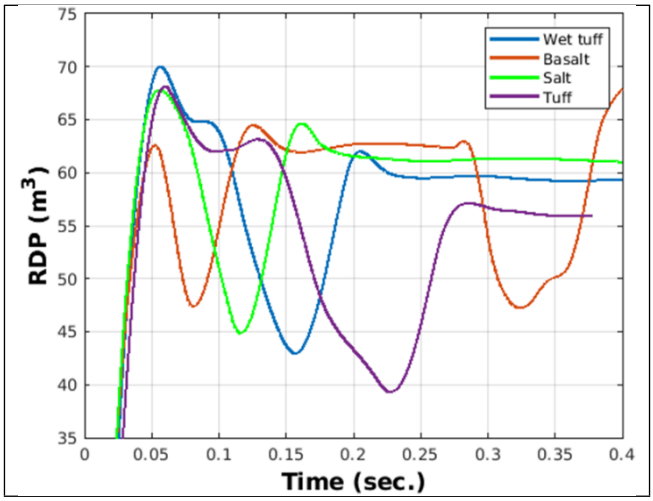

Figure 19. RDP versus time for a tracer at 300 m range, for four different ground materials. Here, the GEO strength model with 0.05 kb yield strength is used and the explosive charge is COMP-B. As described in the text, the basalt response after ~0.3 sec. is

the effect of reflections from the right boundary. Alternatively, we can stop the basalt runs earlier than the other cases.

In Table 11, we summarize the peak RDP, radial velocity, and radial displacement values for various geologic materials. As noted, the peak values for basalt are chosen for times below 0.15 sec, because of the basalt response discussed previously. There are clear variations in peak radial velocity and displacement at 300 m range among the various geologic materials. Wet tuff results in the largest final cavity size and basalt the smallest, but all values are within 1 m/kt$^{1/3}$ of each other.

Table 11. Peak RDP, radial velocity, and radial displacement along with final scaled cavity radius for various geologic materials.

Material	Peak RDP (m^3)	Peak Radial Velocity (m/s)	Peak Radial Displacement (m)	Cavity Scaled Radius (m/kt$^{1/3}$)
Wet tuff	69.8	0.27	0.0026	22.2
Basalt†	62.7	0.16	0.0014	21.3
Salt	67.6	0.22	0.0020	21.8
Dry tuff	68.1	0.31	0.0036	21.8

† For Basalt, we decided to report peak values that occur before 0.15 sec.

Figure 20 shows the peak radial velocities versus scaled range for the various geologic materials being studied here. The figure also includes the line for the tracer at 300 m range (scaled range of 1144.7 m/kt$^{1/3}$). Except for dry tuff, which shows a linear response (in log-log space), the other materials show linear responses with two different slopes. Wortman and McCartor (1985) show the peak particle velocity for chemical (TNT and pentaerythritol tetranitrate, i.e., PETN) and nuclear explosions in salt. They show peak velocities around 0.1 m/sec for salt. Denny (1985) extrapolated the free-field data for dry tuff and shows a velocity of ~0.2 m/sec near ~1100 m/kt$^{1/3}$. Our simulated peak velocities that vary from 0.16-0.31 m/sec at 1144.7 m/kt$^{1/3}$ is in the range of values reported for previous underground explosions.

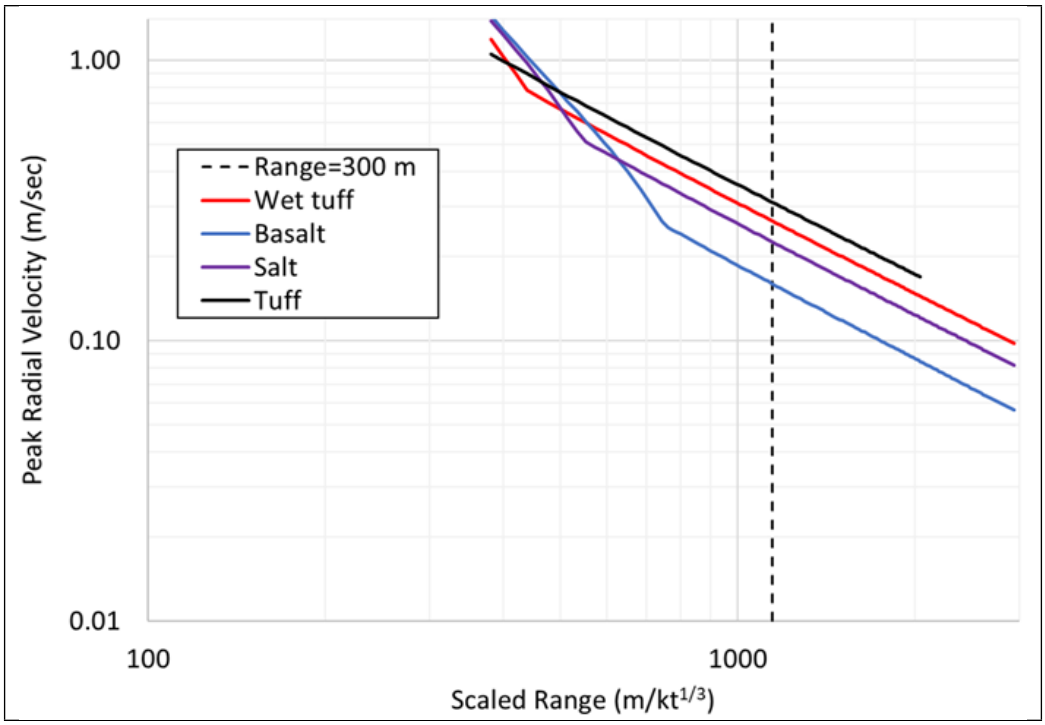

Figure 20. Peak radial velocity versus scaled range for four different geologic materials being examined here. The dashed vertical line represents the scaled range for the 300 m location, where we compare the RDP results. The peak radial velocities at that location for the four materials examined here are ~0.15-0.3 m/sec, with basalt having the lowest and dry tuff having the highest peak velocities.

7. EXPLOSIONS IN CAVITIES

Up to this point, all our simulations consisted of tamped explosions. Next, we discuss the results for explosions in air-filled cavities. As in the last few cases, we use our baseline wet tuff as the ground material, explosive is COMP-B (detonated at the cavity center), and the strength model is GEO with a yield strength of 0.05 kb. Figure 21 frames a through c show the initial setup for the three 11-m radius air-filled cavities, namely, spherical, hemi-spherical, and cylindrical. As noted in the figure caption, the height of the cylindrical cavity is such that the cylindrical and spherical cavities have the same volume. Naturally, the hemispherical cavity is smaller in volume. Frames d through f in the same figure show the final cavity shape at the end of the simulations, i.e., t=0.5 sec. Clearly, the overall original shapes/sizes of the cavities have been maintained. Again, in our analyses the resulting explosive gases (and in these cases mixed air and explosive gases) do not escape the cavity.

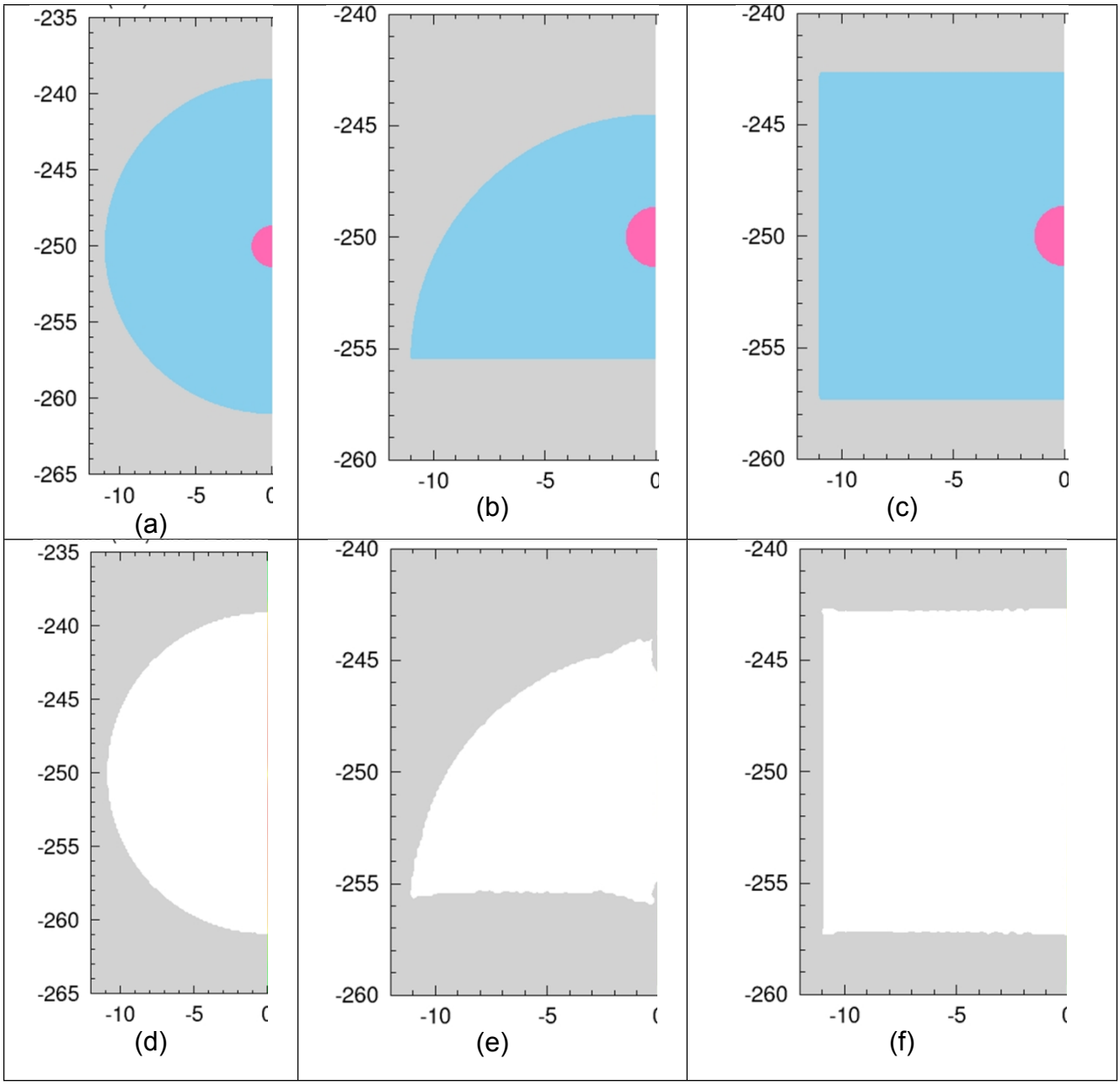

Figure 21. Underground explosions of 18-t TNT equivalent COMP-B in air filled cavities at DOB=-250 m. Initial conditions for (a) 11 m radius spherical cavity, (b) 11m radius hemi-spherical cavity, and (c) 11x14.67 m cylindrical cavity. Note the different scaling for the spherical cavity example. The radius of the cylindrical cavity is 11 m and the height of 14.67 m was chosen so that the spherical and cylindrical cavities have the volume. Gray background is the ground material, blue is the cavity air, and hot pink is the explosives. The final cavity shapes at t=0.5 sec. for (d) spherical, (e) hemi-spherical, and (f) cylindrical cavities show little to no change in the cavity shape. For clarity we have removed the mixed air and explosive gases in the cavity to focus on the final cavity shape (i.e., the white color for images (d)-(f)).

Figure 22 compares the RDPs for the three air-filled cavity cases, at 300 m range. Clearly, the spherical and cylindrical cavities result in small RDP values and have similar responses. Moreover, the RDPs have low amplitude, high-frequency (sinusoidal-looking) responses. Compared to the tamped cases, the RDP values for the spherical and cylindrical cavities are much lower. The similarities (in the RDP magnitudes) for the spherical and cylindrical cases are likely because the explosions occur in the same volume. The explosion in the hemi-spherical cavity, on the other hand, shows an RDP response that, in general, is like our tamped case, i.e., rise to peak, followed by a drop to a minimum and finally another second peak before settling into a nearly steady signal, albeit with the overall RDP size for the hemi-spherical cavity much smaller than its tamped counterpart. We think the reason for the hemi-spherical cavity resulting in larger RDP than the spherical or cylindrical cavities is that the overall volume of the hemi-sphere is smaller than that of the sphere (or cylinder). Murphy et al. (1997) analyzed a series of Soviet-era high-explosive cavity decoupling tests in a mine. They state chemical explosions at 290 m depth in limestone are *essentially fully decoupled in spherical cavities with scaled cavity radii larger that about 27 m/kt$^{1/3}$*. The scaled radius for our spherical cavity is ~42 m/kt$^{1/3}$ that is ~1.5 times larger than the condition reported by Murphy et al. (1997) . By this criterion, our RDP signals for the spherical cavity would represent a fully decoupled signal. Another statement made by Murphy et al. (1997) is that for a scaled cavity radius of 27 m/kt$^{1/3}$, the decoupling is independent of the cavity shape for cylindrical cavities of 6-12 length-to-width ratio. We note that the length-to-radius ratio of our cylindrical is ~1.3 and yet our RDP signal for cylindrical and spherical are like one another. For a 100-ton tamped nuclear detonation in salt, Patterson (1965) reports a peak potential (RDP) of 80 m^3, he scaled from the Salmon (5-kt) tamped experiment. He also reports the RDP for a 100-ton nuclear detonation in a 14.5 m cavity as 0.45 m^3, i.e., a ~99% reduction in RDP from the tamped case. We also a see a reduction of ~98% between our tamped run versus the case in a 11-m radius cavity.

Bottom line is we need to perform Salmon-like simulations and perform seismic analyses, e.g., using the axiElasti tool, Preston (2017), before making more definite judgements about decoupling results. We must note, while not shown here, we performed a simulation for a hemispherical cavity of R=13.86 m, which has an equivalent cavity volume to those of the spherical and cylindrical cavities discussed here. We found that the resulting RDP signal to be closer to those of spherical and cylindrical cases (shown in Figure 22) with a peak RDP around 1.5 m^3. In other words, when the overall cavity volumes are the same, the resulting RDPs are also nearly the same.

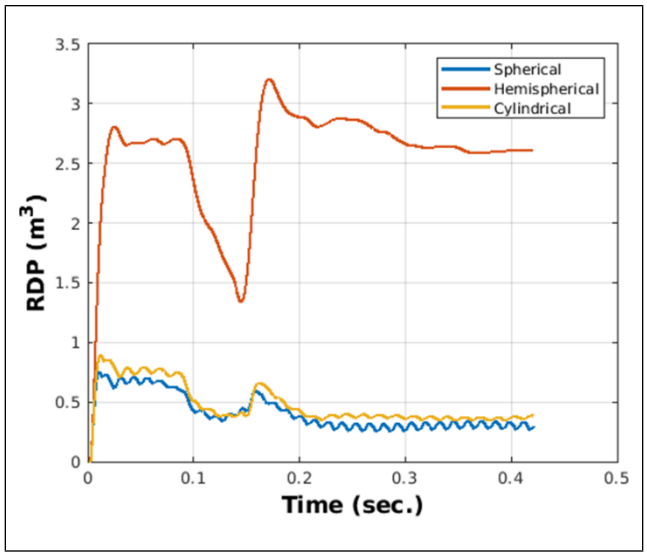

Figure 22. RDP histories at 300 m range for explosions in air-filled cavities. Spherical and cylindrical cavities show nearly similar responses with small RDP values, likely because for both cases the cavities are of the same volume. The hemispherical cavity case shows larger RDP values than the other two cases, since it occurs in a smaller volume. Note that for the equivalent fully tamped case (wet tuff case in Figure 19), peak RDP is 69.8 m^3.

Figure 23 compares the peak radial velocities for tamped and air-filled cavities as a function of scaled range. We note that for the cavity cases, we placed additional tracers that start at the cavity wall (i.e., r=11 m). That is why the scaled range for the cavity cases starts at ~40 m/$kt^{1/3}$. While for all cases, again, there is a nearly linear drop (in log-log scale) for particle velocity versus scaled range, and the air-filled cavity cases show, as expected, smaller peak velocities.

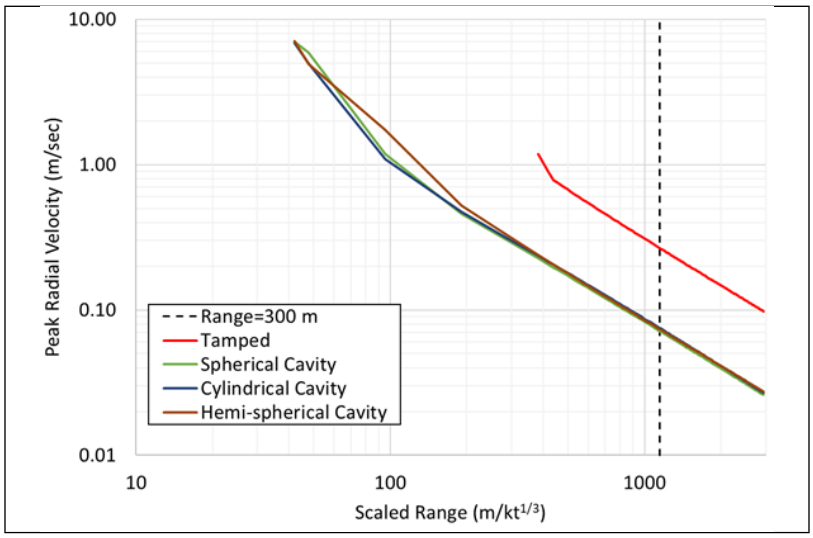

Figure 23. Peak radial velocity versus scaled range for tamped COMP-B explosion compared to those in air-filled spherical, hemi-spherical, and cylindrical cavities. The dashed vertical line represents the scaled range for the 300 m location, where we compare the RDP results.

8. CONCLUSION AND RECOMMNEDATIONS

In this work, we used the CTH shock physics code to simulate the detonation of 18 tons of chemical explosives (COMP-C4 and COMP-B) at a depth of 250 m below the ground surface. Most of the simulations encompassed tamped explosions, although we also examined the effects of three different air-filled cavity shapes. Our CTH model used the two-dimensional axisymmetric geometry along with the AMR. AMR is necessary since our problem domain is on the order of 1-2 km. We used the JWL EOS to model the explosive burn. Using the concept of reduced displacement potential (RDP) as the metric, we compared the various results to better understand the potential uncertainties associated with various model parameter. *However, as we noted earlier in the report, this work is not an uncertainty quantification study*.

8.1. Key Conclusions

- RDP response over time is a convenient metric, used as a surrogate for the resulting seismic signals from an underground explosion. The primary shortcomings of using the RDP are that analysis must be done at a so-called "elastic radius" and it assumes a homogeneous Earth. However, it is possible that ground continues to behave non-elastically, even at far enough distances from the explosion, where the RDP shows a "converged" response.
- Understanding the limitations of the RDP metric, we found that a lower first peak in RDP generally is akin to material being strong and that a smaller RDP (stronger ground material) results in a smaller final cavity for tamped explosions.
- We found the final cavity size formed in tamped explosions is inversely proportional to the yield strength of the geologic material. For instance, using the Geological-yield strength model (GEO) for COMP-C4 explosions in wet tuff results in a ~31 $m/kt^{1/3}$ scaled cavity radius for 0.01 kb yield strength and a ~7 $m/kt^{1/3}$ scaled cavity radius for a 5 kb yield strength. A good understanding of the strength properties of the geologic material is then is critical to accurate prediction of far-field seismic response.
- The choice of slope parameter (DYDP) in the GEO model that controls the degree of non-linearity (DYDP<0, linear model and DYDP>0 nonlinear model) does not greatly affect the RDP magnitude, for the same material and yield strength.
- A limited mesh resolution study showed little variations in RDP and we found a 12.5 cm resolution as "appropriate" for our simulations. However, since we have not performed a full convergence study, we must study the effects of mesh resolution in our future studies. We note that our mesh resolution study only considered the GEO model for a single yield strength and fracture pressure, for a wet tuff.
- For the GEO model, the choice of fracture pressure did not appear to greatly affect the RDP response.
- For the same material, yield strength, fracture pressure, and using the GEO model, an 18-t COMP-B explosion results in a peak RDP that is ~6% lower than a COMP-C4 explosion of the same yield.
- Using the Johnson-Cook strength model, that includes five parameters, has pronounced effects on the RDP response and thus the final cavity radius. The *bottom line is that choice of strength model and its parameters have major effects on the far-field ground response.*

Without appropriate experimental data, it is difficult to judge which model and/or parameter combinations are better than another.

- Cavity formation for these tamped chemical explosions is generally due to mechanical (kinetic) movement of the ground material, as we did not find any material melting even near the source.

8.2. Recommendations

There is currently a lack of dynamic strength and fracture data for underground chemical explosions. To test existing strength and damage models (and perhaps develop new models), and more importantly, to validate our nonlinear models, we need access to data beyond the classic static tests. Given the complex (e.g., highly heterogenous) nature of geologic materials, it is generally difficult to design such experiments. As a result, we may be able to initially use the existing data from historic experiments, e.g., those performed in salt dome as a part of Cowboy series, and attempt to fit our models until we achieve reasonable match between the observations and simulations. Alternatively, identifying other *in situ* data collected in recent experiments to see, for instance, if we can match the acceleration data.

This study did not address the effect of porosity and pore compaction and their effects on RDP (or seismic) signals. Future work should extend our current study to include the effect of pore crush. Pore crush models are included in CTH and include additional material-dependent parameters, which will increase the dimensions of our uncertainties.

We also need to perform a limited study of the effects of material Poisson's ratio and melt temperature on the RDP response. While we do not think the melt temperature will alter our current results, Poisson's ratio, mainly because Poisson's ratio plays an important role in the constitutive model and will affects the resulting yield and flow stresses in the problem.

Among the three strength models examined in this study, our limited parametric study of the Johnson-Cook strength model showed the differences in RDP for different values of constants in this model. In addition, we did not focus on the variations of the damage (fracture) model parameters in Johnson-Cook. It would be worthwhile to extend our parametric study of both the strength and fracture models and examine their effects on the seismic signals. Our suggestion is to include a set of tracers for use in Time Varying Boundary Conditions approach used in AxiElasti and simulate more realistic seismic than those produced by the RDP approach.

Finally, the goal of any parametric study should be Uncertainty Quantification (UQ). UQ is useful when simulation results are directly compared to experimental data to determine margins of uncertainty. We suggest a separate study that purely focuses on using experimental data in conjunction with UQ analysis. We will tap into UQ subject matter experts to design the proper statistical approaches for our UQ work.

References

Denny, M.D. "Anelastic Behavior of Tuff." *The VELA Program, A Twenty-five Year Review of Basic Research, Defense Advanced Research Program Agency, Printed in USA, First Printing: 1985.* Ann U. Kerr, Editor. Available from DTIC, 1985. 278-285.

Hertel, E. S. *CTH Reference Manual: The Equation of State Package.* Albuquerque, NM (OUO/ECI): SAND98-0947, Sandia National Laboratories, 1998.

Heusinkvel, M.E. *Calculation on Seismic Coupling of Underground Explosions in Salts, January 20,* . Unlimited Distribution: UCRL-53103, 1981.

Johnson, G. R. and W. H. Cook. "Fracture characteristics of Three Metals Subjected to Various Strains, Strain Rates, Temperatures and Pressures." *Engineering Fracture Mechanics, Vol. 21, No. 1*, 1985: 31-48.

Johnson, G.W., G.H. Higgins, and C.E. Violet. "Underground Nuclear Detonations." *Journal of Geophysical Research, Vol. 64, No. 10*, October 1959: 1457-1470.

Kerley, G.I. and T.L. Christian-Frear. *Sandia Equation of State Data Base: SESLAN File.* Albuquerque, NM: SAND93-1206, Sandia National Laboratories, 1993.

Latter, A.L., E.A. Martinelli, and E. Teller. "Seismic Scaling Law for Underground Explosions." *Physics of Fluids, Vol. 2, No., May-June,* , 1959: 280-282.

Latter, A.L., R.E. LeLevier, E.A. Martinelli, and W.G. McMillan. "A Method of Concealing Underground Nuclear Explosions." *Journal of Geophysical Research, Vol. 66, No. 3*, March 1961: 943-946.

Murphy, J.R., I.O. Kitov, N. Rimer, V.V. Adushkin, and B.W. Baker. "Seismic characteristics of cavity decoupled explosions in limestone: An analysis of Soviet high explosive test data." *Journal of Geophysical Research, Vol. 102, No. B12*, 1997: 393-405.

Patterson, D. W. *Nuclear Decoupling, Full and Partial, March 26,* . UCRL-1232, 1965.

Poppeliers, C., Wheeler, L.B., and L. Preston. "The Effects of Atmospheric Models on the Estimation of Infrasonic Source Functions at the Source Physics Experiment." *Bull. Seis. Soc. Am. 110(3)*, 2020: 998-1010.

Preston, L., M. Eliassi, A. Gullerud, and C. Poppeliers. "Nonlinear Effects on Linear Seismic Source Inversions from Simulations of Underground Chemical Explosions." *Seism. Soc. Am. 2019 Annual Meeting Abstracts*, 2019.

Preston, L., M. Eliassi, and C. Poppeliers. *Programmatic Advantages of Linear Equivalent Seismic Models.* Albuqueque, NM: Sandia Report, SAND2021-10201, Official Use Only: Exemption 7. Law Enforcement, 2021.

Preston, L.A. *Nonlinear to Linear Elastic Code Coupling in 2-D Axisymmetric Media.* Albuquerque, NM: SAND2017-8848, Sandia National Laboratories, 2017.

Preston, L.A., D.F. Aldridge, and N.P. Symons. "Finite-Difference Modeling of 3D Seismic Wave Propagation in High-Contrast Media." *Soc. Expl. Geophys. 2008 Annual Meeting Extended Abstracts*, 2008.

Schmitt, G., - D.A. Crawford, E.N. Harstad, D. M. Hensinger, K. P. Ruggirello. *CTH User's Manual and Input Instructions, Version 12.0, CTH Development Projects.* Albuquerque, NM, April 20, 2017 (OUO/ECI): Sandia National Laboratories, 2017.

Schultz, R.A. "Limits on Strength and Deformation Properties of Jointed Basaltic Rock Masses." *Rock Mech. Rock Engng. 28(1)*, 1995: 1-15.

Wortman, W.R. and G.D. McCartor. "Analytic Approaches to Linear and Nonlinear Attenuation." *The VELA Program, A Twenty-five Year Review of Basic Research,*

Defense Advanced Research Program Agency, Printed in USA, First Printing. Ann U. Kerr, Editor. Available from DTIC, 1985. 389-398.

DISTRIBUTION

Email—Internal

Name	Org.	Sandia Email Address
Lauren Wheeler	08913	lwheele@sandia.gov
Technical Library	01977	sanddocs@sandia.gov

This page left blank

This page left blank

Sandia National Laboratories is a multimission laboratory managed and operated by National Technology & Engineering Solutions of Sandia LLC, a wholly owned subsidiary of Honeywell International Inc. for the U.S. Department of Energy's National Nuclear Security Administration under contract DE-NA0003525.